FINAL REPORT

NEUP 13-5408, DUNS: 042629816

Under Prime Contract No. DE-NE0000728

Lower Length Scale Characterization and Validation of Formation and Stability of Helium Bubbles in Nano-structured Ferritic Alloys under Irradiation

Prepared by:

Dr. Huijuan Zhao (PI) (hzhao2@clemson.edu)[1]

Dr. Di Yun (co-PI) (diyun@anl.gov)[2a]

Dr. David Hoelzer (co-PI) (hoelzerd@ornl.gov)[3]

Yingye Gan[1]

[1]Mechanical Engineering

Clemson University

Clemson, SC, 29634-0921

[2]Nuclear Engineering Division

Argonne National Laboratory

9700 S Cass Ave B109, Lemont, IL 60439

[3]Materials Science & Technology Division
Oak Ridge National Laboratory
P.O. Box 2008, Oak Ridge, TN 37831-6136

Jan 30, 2018

[a] Dr. Yun is now associate professor at Xi'An Jiao Tong University, Xi'An, China

Table of Contents

1. Executive Summary

In order to extend the operating license of current light water reactors (LWRs) in the United States and other countries to as many as 80 years or longer, it is demanding to identify potential materials for many of the internal structural components and fasteners. We proposed that 14YWT iron alloy can be adopted in such applications with its excellent material properties, such as high-temperature strength, low creep rate, and high irradiation resistance. Application with 14YWT would improve the void/helium swelling characteristics of the LWR fuels, extend the burn-up limits with the tolerant temperature up to 800^{o}C and reduce the hydrogen production. One key feature of 14YWT material property enhancement is the ultrafine high density of 2-4nm Y-Ti-O enriched nanoclusters (NCs) within the 14YWT iron matrix. The NCs can effectively pin the ultra-fine grain boundaries and dislocations, which significantly enhance mechanical properties of the alloy. Moreover, these nanoclusters remain stable with no coarsening after a large dose of ion irradiation. After ion irradiation, the helium bubbles are observed extremely uniform in size (1nm) and quite homogeneously distributed within the 14YWT matrix, which indicates that the microstructure of 14YWT remains remarkably tolerance to radiation damage. However, there is a lack of understanding of 14YWT both theoretically and experimentally in order to understand the mechanism behind the material property enhancement and to further develop and design a new generation of advanced structural material for current LWR applications and future fusion applications.

In this project, we performed theoretical and experimental characterizations of 14YWT in the following aspects: 1) we proposed and developed an Internal Strain Induced Formation (ISIF) model to describe the formation, growth, and stability of Y-Ti-O enriched nanoclusters within 14YWT. We further validated the ISIF model by applying it to the Y-V-O enriched nanoclusters within Eurofer. It indicates that the proposed ISIF model can be further adapted to design new advanced material with the capability of NC formation and growth. 2) We investigated the mechanism of formation and stability of helium clusters within 14 YWT matrix, not only close to the Y-Ti-O enriched nanocluster but also close to the TiN/C nano-precipitates (NP). We elucidated the helium bubble interaction with the NCs and NPs and identified the preferred sites of their growth. 3) We further investigated the strain effects to the growth of helium bubbles as well as the mechanical properties of 14YWT, which partially mimicked the real operating conditions of 14YWT if adopted in the structural material applications. 4). We experimentally investigated the role of nanoclusters in the mechanical property enhancement of 14YWT both at room temperature and elevated the temperature. We identified the role of NCs and NPs in the dislocation migration and elastic anisotropy of the 14YWT, which proves the key role of NCs in the material property enhancement of 14YWT.

The significance of this research as followings. First, determining the interaction between helium gas bubbles and nanoparticles in 14YWT can provide new and fundamental knowledge to further understand the material properties of 14YWT, especially the formation and stability of Y-Ti-O enriched nanoclusters and their contribution to the improved material properties of 14YWT.

Understanding the role of Y-Ti-O enriched nanoclusters and their contribution to the dislocation evolution and internal stress distribution can prove the importance of Y-Ti-O enriched nanoclusters in the mechanical property enhancement of 14YWT. We can then use this new knowledge to design new alloys with high-density nanoparticles to increase mechanical strength, hardness, irradiation resistance, and the operational temperature range of materials, especially in extremely harsh situations. Next, the high-temperature strength, stability and irradiation resistance make 14YWT a potential cladding material for LWR applications. Even though the working temperature of LWR is around 300^{o}C, using 14YWT as a cladding material can provide power plant operators with enough time and opportunity to minimize the damage and prevent severe disasters, such as Fukushima Daichi, from happening again. Long-term benefits of optimizing 14YWT for in-core use will allow utilities to operate their reactors with greater efficiency and lower maintenance, inspection and repair costs.

2. Objectives and Accomplishments

2.1 Objectives and Accomplishments

The comparison between project objectives and project accomplishments are listed in Table 1. The detail project activities and technical narratives are reported in the following sections.

Table 1: Objectives and Accomplishments

Objectives	Accomplishments
1. Theoretical study about the mechanism of formation and stability of helium bubble within the 14YWT matrix	
1.1 Understand the formation and stability of nano-particles within iron matrix through first principles theory calculations.	An internal strain induced formation (ISIF) model has been proposed to elucidate the formation, growth, and stability of the nanoclusters. The ISIF model has been adopted to successfully predict the nanocluster size and oxidation rate relation of Y-Ti-O enriched nanoclusters in 14YWT and Y-V-O enriched nanoclusters in ODS Eurofer. The ISIF model can be adopted for future advanced nanostructured ferritic alloy development for harsh environment applications.
1.2 Understand the interaction between helium and nano-clusters/particles within 14YWT through first principles theory calculations	A systematic first principles theory calculations have been performed to establish the fundamental understanding of helium clusters interaction with Y-Ti-O enriched nanoclusters and TiN/TiC nano-precipitants within 14YWT. The helium displays a strong affinity to the oxygen:vacancy pair. The helium atom tends to join the helium cluster through the directions away from the solute atoms (Ti and Y). At the same time, He clusters show the tendency to expand in the directions away from Ti and Y atoms.

	Our theoretical understanding of the He cluster formation and growth is consistent with the recent experimental observations.
1.3 Propose a theoretical model to elucidate the mechanism of formation and stability of helium bubbles within 14YWT matrix	A growth criterion has been proposed based on the elastic instability strain of the perfect iron lattice in order to determine the maximum size of helium cluster near one vacancy site. The prediction of helium cluster size based on the proposed growth criterion matches well with the results from other non-equilibrium first principles theory calculations.
1.4 Adopt the proposed model to determine the stability of helium bubbles when the 14YWT matrix is under various external strain conditions	The presence of tensile initial strain is identified to be able to promote the trapping of helium, while the compressive initial strain weakens the nanoclusters attraction to helium. Regardless of initial strain, vacancies and O:Vac pairs in 14YWT always act as trapping sites of helium atoms Such understanding of helium solution of 14YWT to external strain is of great significance to its measuring, testing, and design in future applications. The existence of solute atom Ti and impurity atom He can induce hardening of Fe matrix in 14YWT under strong constraints. At the same time, helium atoms can degrade the material integrity with local interaction, especially with the removal of strong stress constraints. The polycrystalline elastic parameters for Fe lattice under various initial strain states have been obtained, which can be adopted as the input for continuum scale studies such FEA modeling of 14YWT.
2. Experimental characterization of 14YWT	
2.1 Re-characterize the gas content in the bubbles/cavities with high resolution STEM techniques and converged beam EELS analyses. Identify the relation between bubbles/cavities and nano-particles within 14YWT matrix	The high-energy synchrotron X-ray diffraction technique has been adopted to study the time-resolved lattice strain and dislocation density development during deformation of 14YWT. The nanoclusters in 14YWT are invisible in the measurement due to their non-stoichiometric nature. The major strengthening mechanism in 14YWT is identified to be dispersed-barrier-hardening due to the ultra-fine but sharable nanoclusters. Based on Bergström's dislocation models, dislocation density evolutions were modeled with two different assumptions: (1) dislocation mean free path was strain independent (i.e. constant value of s); and (2) dislocation mean free path was strain dependent (i.e. s(ε)). Although both models provide good consistency with the

	dislocation density interpreted from X-ray measurements, only the model with strain dependent s has been proved to capture the phenomenon of slightly dislocation density decreasing after sample necking.
2.2 Perform in situ straining tests to characterize the smooth bubble/cavity motion with a particular emphasis on the possible coarsening of the helium bubble/cavities	The in-situ high-energy synchrotron uniaxial tensile tests have been conducted on various material samples at room temperature and elevated temperature conditions. An increase in the elasticity anisotropy in all of the materials studied with an increase in temperature. An analysis of the intergranular strain of 14YWT-sm13 indicated a higher resistance to temperature softening compared to 9YWTV. A further analysis of the strengthening factors indicated differences in the applied and mean internal stress. This variation was due to a higher temperature dependence of the nanoparticle strengthening for 14YWT-sm13 compared to 9YWTV, particularly at the higher temperatures.

2.2 Other Achievements

- One Ph.D. student has been fully supported by this project and successfully graduated in May 2017. Three graduate students have been partially supported by this project.
- Throughout the project period, three journal papers have been published, nine conference presentations (oral and poster) have been given at TMS, MRS, NuMat and etc. Three invited talks has been given at ANL, the University of Washington at Seattle and etc. Currently, there is one journal manuscript under review and one journal manuscript under preparation.
- Multiple general user proposals have been submitted to the Advanced Photon Source (APS) facility. 48 hours beam time has been awarded. Two journal papers are published based on this effort.
- Other than the accomplishments listed in the table above, the helium interaction at the Fe-TiN interface has been investigated. Helium is observed to tend to locate at the Fe-TiN interface by creating large distortion to the nearby Fe atoms.

2.3 Impacts

The significance of this research is three-fold. First, determining the interaction between helium gas bubbles and nanoparticles in 14YWT can provide new and fundamental knowledge to further understand the material properties of 14YWT, especially the formation and stability of Y-Ti-O enriched nanoclusters and their contribution to the improved material properties of 14YWT.

We can then use this new knowledge to design new alloys with high-density nanoparticles to increase mechanical strength, hardness, irradiation resistance, and the operational temperature range of materials, especially in extremely harsh situations. Next, using both the analytical formulation about the helium bubble formation and stability and the interaction with nanoparticles in 14YWT under relaxed and strain conditions, we expect to systematically include 14YWT as a cladding material for design and optimization of current LWRs and future fusion energy systems. Finally, the high-temperature strength, stability and irradiation resistance make 14YWT a potential cladding material for LWR applications. Even though the working temperature of LWR is around 300^{o}C, using 14YWT as a cladding material can provide power plant operators with enough time and opportunity to minimize the damage and prevent severe disasters, such as Fukushima Daichi, from happening again. Long-term benefits of optimizing 14YWT for in-core use will allow utilities to operate their reactors with greater efficiency and lower maintenance, inspection and repair costs.

3. Project Activities

The research activities involved in this project can be divided into two major efforts: (1) theoretical modeling and characterizations of 14YWT, including the model to describe the formation and stability of nanoclusters within 14YWT; the helium cluster interaction with nanoclusters within 14YWT and its growth criteria; the helium cluster interaction with nanoparticles within 14WYT; and the strain effect to the growth of helium clusters within 14YWT. (2) experimental characterization of 14YWT through high-energy X-ray synchrotron tests, including the dislocation density evolution and modeling of 14YWT and other DOS materials at room temperature, and the role of the ultrafine nanoclusters to the mechanical property enhancement of 14YWT at both room temperature and elevated temperatures. In the following, the key findings in each sub-projects will be listed and explained.

3.1 ISIF model: the formation, growth, and stability of nanoclusters within NFAs

One of the most important features of advanced nanostructured ferritic alloys such as14YWT and ODS-Eurofer is the high density uniformly distributed ultra-fine nanoclusters (NC) within the iron matrix (Fig. 1(a)[b]). These NCs do not coarsen at an elevated temperature which plays an important role in the strength enhancement and irradiation resistance. Since the helium bubbles generated after ion irradiation show a homogeneous distribution within the iron matrix with an extremely uniform in size (1nm), we think the NCs play an important role to trap helium in fine bubbles. Thus, it is important for us to understand the formation and stability criteria of NCs.

[b] D. T. Hoelzer, J. Bentley, M. A. Sokolov, M. K. Miller, G. R. Odette, M. J. Alinger, "Influence of particle dispersions on the high-temperature strength of ferritic alloys", J. Nucl. Mater, 367-370, 166-172 (2007)

Hypotheses

We proposed an internal strain induced formation (ISIF) model to describe the formation, growth, and stability of nanoclusters within NFAs. In the ISIF model, we assume that the nanocluster structure is coherent with the Fe BCC lattice. Since O:Vac pairs are distributed randomly in the NCs (Fig 1(b)), the atomic ordering of NCs is essentially amorphous. Due to the strong solute-O:Vacancy (O:Vac) binding, the only available sites for the solutes in the NCs are the neighboring sites of O:Vac pair (the 1st and 2nd site groups in Fig. 1(c)). Therefore, the NCs can be viewed as an ensemble of interacting units (shown as the solid blue square boxes in Fig. 1(b)). Each unit consists of an O:Vac pair and its nearest neighbor solute atoms. Therefore, the averaged O-binding energy of a NC can be defined as

$$E_b^{\mathrm{NC}}(\mathrm{O}_1) \cong E_b(\mathrm{O}_1) + \frac{1}{2}\sum_{i=1}^{N_1} f_i E_{int}(\mathrm{O}_i), \quad (1)$$

where $E_b(\mathrm{O}_1)$ is the O-binding energy of an isolated unit, N_1 is the number of its neighboring sites, f_i is the probability that the site i is occupied by an O:Vac pair and $E_{int}(\mathrm{O}_i)$ is the averaged interaction energy over the possible O:Vac pair orientations at site i. In this model, the f_i factor is site independent and represents the O concentration in the cluster. N_1 and $E_{int}(\mathrm{O}_i)$ are site dependent and vary due to different surface termination when the isolated unit is near the cluster surface. In order to cease the growth of the NC, the following criteria needs to be satisfied,

$$\mathrm{f(n)}(\mathrm{E_B} - \mathrm{E_S}) \geq (\mathrm{E_0} - \mathrm{E_S}), \quad (2)$$

where $\mathrm{E_S}$ and $\mathrm{E_B}$ are the averaged O-binding energies (per O) of the interfacial region and bulk region of the NC, respectively. $\mathrm{E_0}$ is the O-binding energy in the matrix. $\mathrm{f(n)} \in (0,1)$ is a parameter related to NC size, in which n is the number of unit cells. This criterion means that: (1) $\mathrm{E_S}$ is higher (more negative) than $\mathrm{E_B}$, and (2) the O-binding energy in the matrix $\mathrm{E_0}$ is located in-

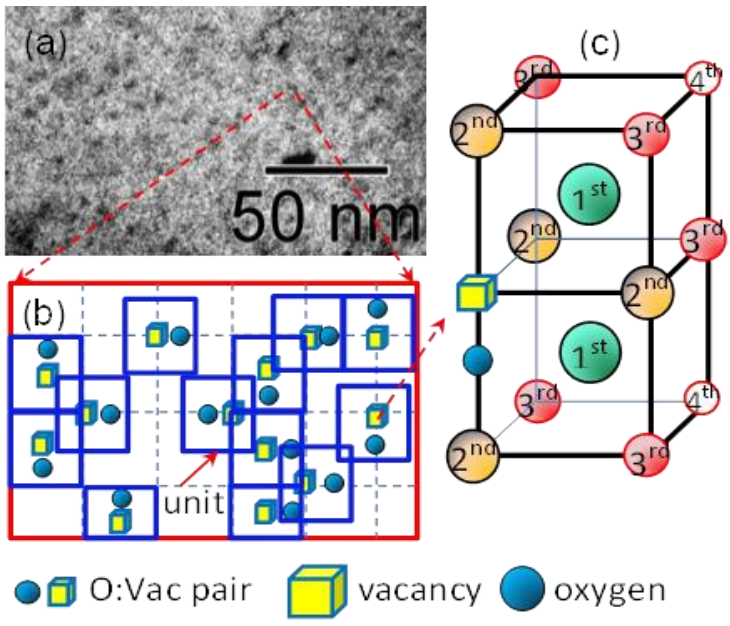

Figure 1 (a) EFTEM image of NCs in 14YWT. (b) Schematic representation for model geometry of units in a single NC. Each unit (blue square) consists of an O:Vac pair with its nearest neighbor solute atoms (not shown in the graph). (c) Schematic representation for solute-O:Vac interactions. The 1st -4th level interactions are when the solute vacancy distance is $\sqrt{3}/2$a (8 positions), a (6 positions), $\sqrt{2}$a (12 positions), $\sqrt{3}$a (8 positions), respectively.

between E_B and E_S. $f(n) \in (0,1)$ can be maintained for any arbitrary shapes of NCs, whereas in the following calculation, we use $f(n) = \frac{(n-1)^3-(n-2)^3}{(n+1)^3-n^3}$ derived from a cubic-shape of NCs.

Approaches

The first principles theory calculations have been conducted through the Vienna *ab initio* simulation package (VASP) to solve the spin-polarized local density equations. The ultrasoft pseudo-potential was adopted with the generalized gradient approximation (GGA). A super cell up to 128 atoms is adopted to represent the Fe matrix in order to reach the convergence of 0.1eV for the interaction energy calculations.

Main Results

This ISIF model has been adopted to evaluate the formation and growth of Y-Ti-O enriched nanoclusters within the 14YWT iron matrix[c]. The essential stability condition of these nanoclusters is found to be the exceptionally low interfacial energy compared with the interior energy of these nanoclusters. The strain energy accumulated within the nanoclusters is mainly from the solute-solute repulsive interaction and the solute-oxygen-vacancy interaction due to the local strain gained from the solute near the lattice site.

In this work, the ISIF model has been further adapted to investigate the formation, growth, and stability of Y-V-O enriched nanoclusters in Eurofer97. We observed that the interaction between a solute atom and O:Vac pair depends on both the solute-vacancy distance and the orientation of the O:Vac pair to the solute atom. Most of the attractive interactions occur when the solute is at the nearest neighboring site of the vacancy site. By definition, most of the solute atoms in NCs are shared by multiple units (or O:Vac pairs). In our calculation, we fixed the solute position at the lattice site to mimic the constraint by the multiple O:Vac environment. Since Y atom has a strong affinity to O:Vac pair, fixing Y atoms at the lattice sites could introduce strong strain energy. A stable unit cell is defined as an O:Vac pair with its neighboring solute atoms, which achieve the maximum magnitude of the binding energy without adding more solute atoms. The main resources of the strain energy are both the solute-solute repulsion and the Y-O:Vac interaction due to the confinement of Y atom at the lattice site. The strain energy due to the close pack solute-solute repulsion is dominant.

After fully understanding the interactions between solutes, O:Vac pairs and units, the formation procedure of NCs can be explained as following. To initiate the nucleation of NCs, the binding energy of O in the nuclei must be lower than the heat of formation of the solute oxide phase. The fragment of a unit then can be attached to the nuclei due to the attractive interaction between solute-O:Vac pair and O:Vac-O:Vac pairs. During the growth of the NCs, the strain energy accumulates within the NCs. The growth of a NC reaches its critical size once the energy

[c] H. Zhao, C. L. Fu, M. Krcmar, and M. K. Miller, "Effect of strain on the stabilization of oxygen-enriched nanoclusters in Fe-based alloys", Phys. Rev. B. 84, 144115 (2011)

change in the overall NC energy due to the addition of units on the interface becomes positive. During this formation procedure, the unit cell can attach to each other mainly due to the strong solute-O:Vac attractive interactions. On the other hand, the resources of the strain energy are mainly from the Y atom shared among the multiple unit cells (fixed at the lattice site) and the solute-solute repulsion between unit cells. Since the growth of NCs is due to the attachment of unit fragments, we assume that all the O:Vac pairs in the matrix are in the unit fragment form, which means it might or might not be attached with a solute atom.

Since the V/O ratio is observed to be ~ 1 in the NCs, the averaged O-binding energy in the matrix E_0 can be set as the O-binding energy of an isolated V-O:Vac pair in Fe, which is -2.33eV. For Y-V-O enriched NCs, we adopt two reference units. R1 is the most energetic stable unit without Y atoms where two V atoms are at the $\frac{1}{2}[11\bar{1}]$ sites of the vacancy site while the O atom is in the $[00\bar{1}]$ direction of the vacancy site. The O-binding energy of R1 is -2.57eV. R2 is R1 unit with Y atom at the $\frac{1}{2}[111]$*the* site of the vacancy site. R2 unit is also at the energetic stable state with the O-binding energy as -3.18eV. By all the interactions we have already studied, the O-binding energy of reference unit R1 and R2 for the Y-V-O enriched NCs are calculated as a function of O-concentration shown in Fig. 2(a). Solid lines with symbols represent E_B, dash lines with symbols represent E_S and the solid black line without symbol represent the O-binding energy in the matrix. The lines with circle symbols are for the R1 reference unit, while as the lines with diamond symbols are for the R2 reference unit. For reference unit R1, when O concentration is in the range of 14-23% (the red line box in Fig. 2(a)), the calculated E_B, E_S and E_0 values are found to satisfy the formation criteria of the NCs. However, for R2 reference unit R2, the formation criteria is satisfied only when O concentration is in the range of 42-67% (the blue box in Fig. 2(a)). In our previous study

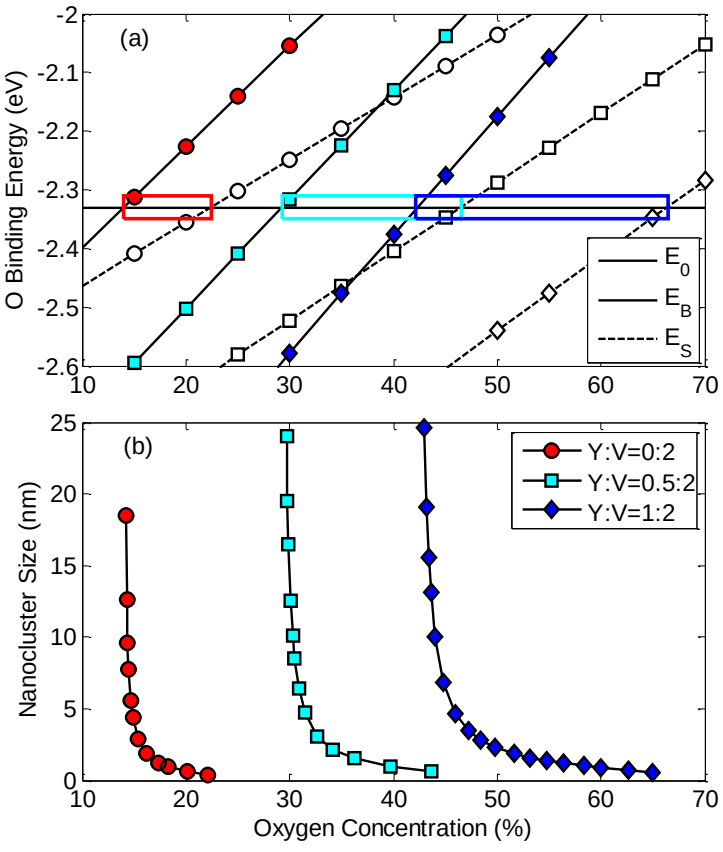

Figure 2 (a) The O-binding energy as a function of O concentration in NCs. (b) The calculated NC size as a function of O concentration in the NCs. Circle symbol for Y:V ratio 0:2, square symbol for Y:V ratio 0.5:2, diamond symbol are for Y:V ratio 1:2.

about the Y-Ti-O enriched NC systems, Y solutes do not have a significant impact on the trends and magnitudes of the O-binding energy. From the prediction of the generalized strain energy model, the NCs can be formed with the oxygen concentration between 35-50% regardless the ratio of Y/Ti. However, in Y-V-O enriched system, Y atoms have a strong impact on the trends and magnitudes of the O-binding energy. The strain energies gained during the formation process are similar between the R1 units and R2 units since there is no difference between the V-V, V-Y repulsive interaction energies. But the O-binding energy of the unit cell is greatly lowered due to the existence of Y atom. So for Y-V-O enriched NCs, the NC size is closely related to both the Y concentration and the O concentrations. The atom composition ratio of Y/V is observed by different research groups and reported as 1:4 ~ 1:2 with the NC size from 1nm to 5 nm. With different Y/V ratio, Fig. 2(b) shows the NC size as a function of the oxygen concentration. No matter what is the Y/V ratio, the NC size decreases from an infinite size dramatically and the vast majority of the NCs with the corresponding O concentration range have the size around 1-5nm. This finding fits the experimental observations quite well[d,e].

Impact

In this task, we proved that the proposed ISIF model is valid in predicting the formation and growth of Y-Ti-O enriched nanoclusters in 14YWT and Y-V-O enriched nanoclusters in ODS Eurofer. It can be further adapted for the nanoclusters formation and stability study in any advanced NFAs.

3.2 Helium cluster formation and growth criteria within 14YWT

In the fusion reactors industry with such a high energy neutron irradiation environment, large numbers of helium atoms are either directly implanted into or produced internally through (n, a) transmutation reactions in the Fe matrix. Due to the low solubility of He atoms in an iron matrix, these He atoms can be easily trapped with the vacancies from the energetic displacement damage to form He bubbles, causing void swelling, blistering and creep rupture of the structural materials, which drastically decrease their service life and mechanical reliability. According to recent experiments, the distribution of He bubbles in irradiated 14YWT is extremely homogeneous and has a strong tendency to concentrate at the nanocluster-matrix interface. Through the combined Transmission Electron Microscopy (TEM) and Atom Probe Tomography (APT) data, researchers have indicated that 48.6% of He bubbles are located on the nanoclusters, 14.4% are at the grain boundary, 12.2% are at the dislocations, 4.4% are at the coarse precipitates ($Y_2Ti_2O_7$ and Ti(N,C)) and the remaining 20% of He bubbles are located within the iron matrix[f]. The size of the

[d] A. A. Aleev, N. A. Iskandarov, M. Klimenkov, R. Lindau, A. Moslang, A. A. Nikitin, S. V. Rogozhkin, P. Vladimirov, and A. G. Zaluzhnyi, "Investigation of oxide particles in unirradiated ODS Eurofer by tomographic atom probe", J. Nucl. Mater, 409, 65 (2011).

[e] M. K. Miller and C. M. Parish, "Role of alloying elements in nanostructured ferritic steels", Mater. Sci and Tech. 27, 729 (2011).

[f] P.D. Edmondson, C.M, Parish, Y. Zhang, A. Hallen, and M.K. Miller, "He bubble distributions in a nanostructured ferritic alloy". J. Nucl. Mater. 434, 210-216 (2013)

bubbles is around 1 nm with the density of 10^{23} bubbles/m^3, similar to the density of NCs. Due to the homogeneous bubble distribution and uniform bubble size, the irradiation-induced damage is significantly reduced in 14YWT. Therefore, in this task, we will elucidate the underlying mechanism of the helium bubble formation and stability near the Y-Ti-O enriched nanoclusters within 14YWT.

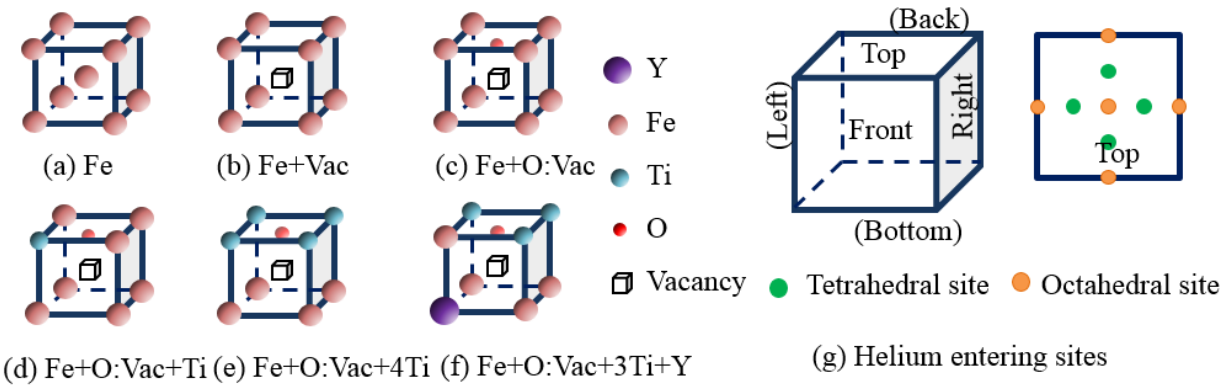

Figure 3. (a)–(f) Schematic atomic configuration of the reference units; (g) The possible entering sites of He on the reference unit during the He cluster growth. The six planes of the reference unit are named top, front, right, bottom, back and left. On each plane, the 5 octahedral sites and 4 tetrahedral sites are presented

Approaches and definitions

We adopt the Vienna ab initio Simulation Package (VASP) to perform first principles theory calculations. The spin-polarized scheme is selected due to the ferromagnetism of a-iron. The Projector Augmented Wave (PAW) pseudopotential is chosen to describe the electron-ionic core interaction. The electron exchange and correction is described with Generalized Gradient Approximation (GGA) and Perdew-Burke-Eruzer (PBE) functionals. The Methfessel-Paxton scheme is selected for the smearing function. The cut-off energy is set to 650 eV for all cases. A supercell of 3×3×3 unit cells (54 Fe atoms with the perfect lattice) is adopted for all of the energetic studies in this work. Within the Monkhorst-Pack scheme, we conduct the convergence study with various k-meshes (3×3×3 to 6×6×6) and select a 3×3×3 k-mesh in the following calculations in order to maintain both the energy accuracy of 0.001eV and the computational efficiency.

Since most of the He bubbles are located on the nanoclusters, at the grain boundary and within the 14YWT iron matrix, we select six reference units to investigate the He cluster nucleation, formation and interaction within the 14YWT matrix, shown in Fig. 3. Figure 3(a,b) denotes the reference units with a perfect lattice and a single vacancy, respectively. Figure 3(c) is the reference unit with the O:Vac pair. Figure 3(d) is the reference unit of an O:Vac pair with one Ti atom, which is the most stable state of the O:Vac pair in the 14YWT matrix. Figure 3(e,f) is the two reference units, which represent the two major local environments of the O:Vac pair within the nanoclusters. In order to energetically investigate the He cluster nucleation and formation behavior, we replace the center unit cell in the super-cell with the reference unit cell listed in Figure 3, respectively, and

add He atoms one by one into the reference unit through all 42 tetrahedral and octahedral interstitial sites, as shown in Figure 3(g). For each configuration, the symmetry of these entering sites has been considered in order to limit the number of calculations. Since the He atom can move easily between interstitial sites within an iron matrix due to the low migration energy barrier (0.06 eV)[g], the newly-added He atom can easily migrate within the super-cell in order to achieve the equilibrium energy state. Due to the various entering sites, multiple numbers of equilibrium configurations can be achieved. In the following discussion, the helium sample entering site (SES) is described with the format of *abg*. *a* is the helium entering plane, which can be F (front), K (back), T (top), B (bottom), L (left), R (right) and A (all). *b* is the helium interstitial site, which can be T (tetrahedral), O (octahedral) and A (all). *g* is the helium interstitial position on each plane, which can be A (all) and C (center), and the plane close to He atom: T (top), B (bottom), L (left), R (right), F (front) and K (back). In this study, all of the calculations are based on the constant volume condition with the lattice constant a_0 = 2.83 Å for a perfect BCC iron lattice. To understand the He cluster formation and growth, we focus on the formation energy and the He trapping energy of each individual configuration. The formation energy is defined as:

$$E_f(\text{ref} + n\text{He}) = E(\text{ref} + n\text{He}) - E(\text{ref}) - nE(\text{He}), \quad (3)$$

where ref + *n*He denotes the reference unit with n number of He atoms in the super-cell; subscript f denotes the formation energy. E(He) = 0.0046 eV is the energy of an isolated He atom in the vacuum space. During the He cluster formation, the He trapping energy is an important parameter to determine whether the n-th He atom can be trapped into the $He_{(n-1)}$ cluster. For the accumulation of the *n*-th He atom, the He trapping energy is defined as:

$$E_{trap}(\text{ref} + n\text{He}) = E_f(\text{ref} + n\text{He}) - E_f(\text{ref} + (n\text{-}1)\text{He}) - E_f(\text{He}_{tetra}), \quad (4)$$

where $E_f(\text{He}_{tetra})$ is the formation energy of a tetrahedral interstitial He within the perfect Fe lattice.

Hypotheses

During the He accumulation within the local environment of the vacancy/O:Vac pair, significant pressure has been produced, causing significant distortion of the local lattice structure. After the local lattice structure reaches its elastic instability, it must conduct plastic deformations (phase transition, dislocation nucleation, etc.) in order to release the pressure, therefore providing more space for the continued growth of the He cluster. Herein, we propose to adopt the elastic instability strain of a perfect BCC Fe lattice as the criteria for the He cluster growth at the vacancy site. In order to determine the elastic instability strain of the perfect BCC Fe lattice, the tri-axial strain-stress tensile test is performed along the [001] direction. The ideal strength is reached at 15% strain, matching well with the published data. Continuing to load after reaching 15% strain will associate the BCC iron lattice with an elastic instability along the Bain path from BCC to FCC.

[g] M. K. Miller and C. M. Parish, "Role of alloying elements in nanostructured ferritic steels", Mater. Sci and Tech. 27, 729 (2011)

Therefore, we adopted 15% as the maximum bond strain to evaluate the maximum number of He atoms in the He cluster growth at the reference units in Figure 3.

Main Results

In our calculation, we found that the He atom prefers the tetrahedral interstitial site with a lower formation energy without vacancy; otherwise, the He atom is trapped in the vacancy as a substitution. With the pre-existing vacancy, the He atom can be easily trapped at the vacancy site. In 14YWT, most of the pre-existing vacancies are occupied by oxygen atoms, but the effect of pre-occupied oxygen at the pre-existing vacancy site on the He trapping behavior is very limited. The He atom still displays a strong affinity to the O:Vac pair in 14YWT.

Let us denote He cluster as He_nX, where n is the number of He atoms in the cluster and X represents the reference unit listed in Fig. 2. If He atoms are gradually added to the reference unit from the interstitial sites, various equilibrium configurations will be reached depending on the entering sites. The magnitude of the trapping energy depends on both the reference unit and the number of helium atoms in the He_nX. With the increasing of *n*, the E_{trap} is significantly reduced. More energy is required for the He_nX clusters' growth near the nanocluster interface than that within the matrix. He prefers to enter the He_nX clusters from the sites away from the solute atoms (Ti and Y). In other words, even though the O:Vac pair performs as the He sink, the Ti and Y atoms impose a blocking effect during the growth of He clusters, preventing the close-by He atom from joining the He cluster centered at the O:Vac pair. More importantly, it is difficult for He atoms to enter the nanocluster and nucleate the He cluster inside the nanocluster, which contains 40% Ti and 10% Y atoms. Therefore, this explains the experimental observations that most of the He bubbles are formed next to the nanoclusters without penetrating inside.

We have calculated the growth of He_nX clusters with n up to 8. With the criterion of negative He trapping energy, the He_nX clusters can continue growth when n = 8. To investigate the local distortion and maximum size of the He cluster, the bond strain variations with the number of He in He_nX clusters are presented in Figure 4. The solid lines with a symbol represent the average bond strain within the reference unit of the super-cell (12 bonds in each reference unit). The dashed lines represent the maximum and minimum bond strain at the corresponding condition. It is clear that with a single vacancy in the iron matrix, the local bond distortion is limited. The maximum number of He atoms in the He cluster is n = 7, since the maximum bond strain exceeds 15% at n = 8. With the O:Vac pair, local bond distortion becomes significant. The maximum number of He atoms in the He cluster is n = 5, shown in Figure 4b. With the major local environment of the O:Vac pair within the nanoclusters (Figure 3d,f), the maximum number of He atoms is reduced to n = 5 and n = 1 for Fe + O:Vac + 4Ti case and Fe + O:Vac + 3Ti + Y case, respectively. The bond distortion increases dramatically after the limit is reached. The maximum bond strain variation can exceed 25%. It is obvious that the existence of other solutes can reduce the size of He cluster associated with a single vacancy, especially the Y atom.

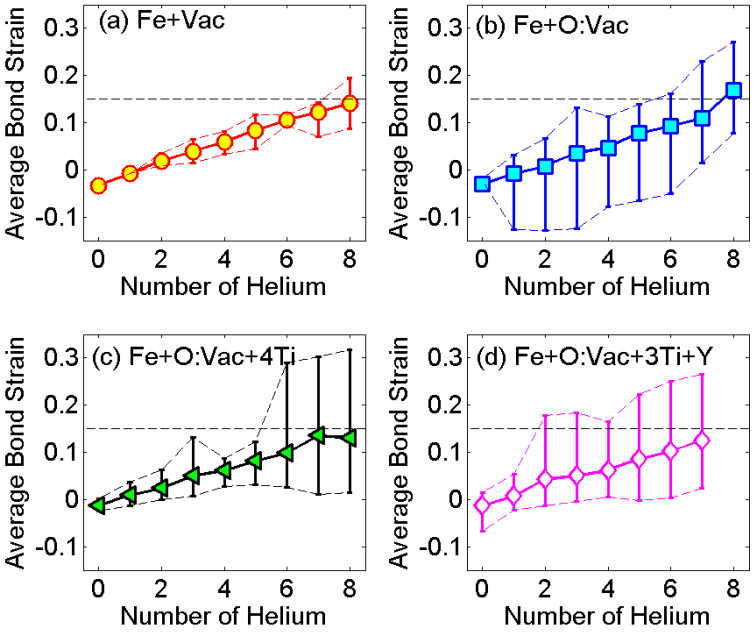

Figure 4. (Color online) Bond length variations in various reference units: (a)Fe+Vac; (b) Fe + O:Vac; (c) Fe + O:Vac + 4Ti; and (d) Fe + O:Vac + 3Ti + Y.

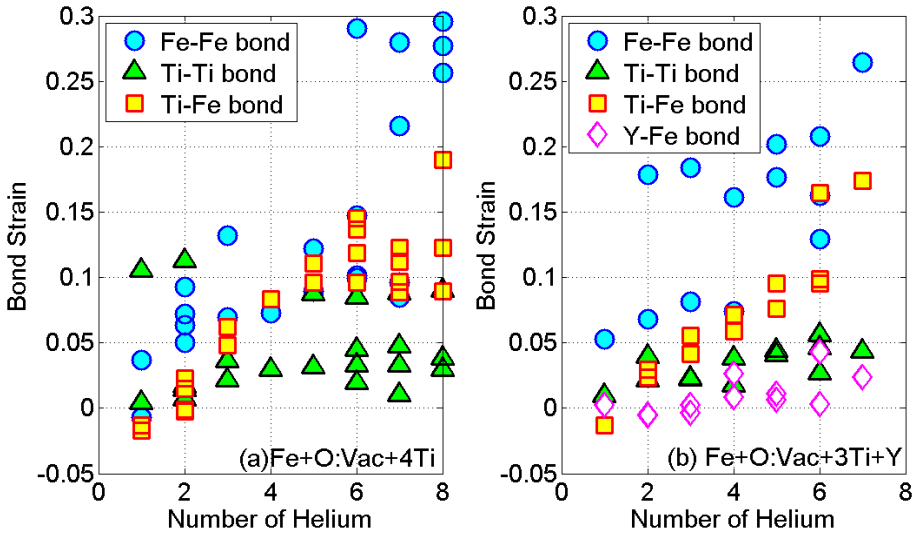

Figure 5. (Color online) (a) bond strain variation of the reference unit of Fe + O:Vac + 4T; (b) bond strain variation of the reference unit of Fe + O:Vac + 3Ti + Y.

In order to understand the significant local distortion in Figure 4c after n = 6 and Figure 4d after n = 2, we further plot the Fe-Fe, Ti-Ti, Ti-Fe and Y-Fe bond strain variations with the number of He atoms, shown in Figure 5. Fe-Fe bonds are much more severely distorted by the He cluster than the other bonds. The strain on Ti-Ti bonds and Y-Fe bonds remains stable during the growth of He cluster. Such results implicate the preference in the nucleation site of the He_nX cluster from the aspect of bond strain variation. He atoms tend to avoid the stronger Ti-Ti bonds during the nucleation process. A He bubble can be easily nucleated on nanoclusters due to the high density

of the O:Vac pair, but will grow in the near-by matrix at the NC-matrix interface without penetrating the NCs. This theoretical finding is consistent with the experimental observation in reference[h].

As we discussed, the initial nucleation and growth of the He bubble mainly depends on the interaction between the He cluster and a single vacancy under various local environments. However, the size of He bubbles after irradiation is also related to the mobility of He atoms in the He_nX cluster. Interstitial He atoms have a very low migration energy of 0.06 eV. The migration of substitutional He is found to be governed by the migration of the Vac-He-Vac complex, with an energy barrier of 1.1 eV[i]. In order to understand the effect of other solutes on the He/He_nX cluster migration in 14YWT, we adopted the nudged elastic band method (NEB) to compute the migration energy of He between the Reference Unit (b) and the Reference Units (b, c, e) shown in Figure 2. We found that the migration energy barrier of the He atom in the Fe + Vac→ Fe + O:Vac + 4Ti path is 0.5 eV higher than that in the Fe + Vac→ Fe + Vac path. The migration energy barrier of He atom in the Fe + Vac → Fe + O:Vac path is 0.2 eV higher than that in the Fe + Vac → Fe + Vac path. Although more quantitative investigations should be done to fully understand the migration behavior of He atoms/He_nX clusters in 14YWT, qualitatively, we find it is more difficult for He atoms to diffuse between two trapping sites with the presence of other solutes. The coalescence of the small He clusters into multiple vacancy-induced He bubbles might be hindered because of the barriers provided by these solutes in the He atom diffusion process. Such impedance produced by these solutes can be a crucial factor in the He bubble size-controlling mechanism in 14YWT.

Impacts

In this work, we found that the O:Vac pair presents similar He trapping behavior with a single vacancy. The He entering site plays an important role in the formation of the He cluster with the presence of other solutes, such as Ti and Y. He atoms tend to enter the He cluster through the directions away from Ti and Y atoms. At the same time, He clusters show the tendency to expand in the directions away from Ti and Y atoms. In order to determine the maximum number of He atoms near one vacancy site, a growth criterion is proposed based on the elastic instability strain of the perfect iron lattice. Our theoretical understanding of the He cluster formation and growth is consistent with the recent experimental observations.

3.3 Helium cluster interaction at the TiN/C-Fe interface

Other than the majority nano-particles: Y-Ti-O enriched nano-clusters, the rest of the nano-particles are mainly in the phase of $Y_2Ti_2O_7$, TiN or TiC, with a relatively larger size of 5-30nm. In the previous task, we have investigated the helium cluster formation and growth mechanism

[h] P.D. Edmondson, C.M, Parish, Y. Zhang, A. Hallen, and M.K. Miller, "He bubble distributions in a nanostructured ferritic alloy". J. Nucl. Mater. 434, 210-216 (2013)

[i] M. K. Miller and C. M. Parish, "Role of alloying elements in nanostructured ferritic steels", Mater. Sci and Tech. 27, 729 (2011)

within 14YWT at various local lattice environments such as perfect iron matrix, iron matrix with vacancy, iron matrix with O:Vac pair and the O:Vac pair surrounded with other solutes such as Ti and Y. In this task, we focused on the helium interaction at the iron-TiN interface. The coarse nano-precipitates such as TiN in 14YWT have the lattice structure of NaCl-type or TlI-type lattice structure, as shown in Fig.6 (a,b). Therefore, we investigate the helium interaction at the Fe-TiN interface, with the consideration of TiN lattice structure, the coherency of the interface, and vacancies.

Approaches and assumptions

To simulate the helium interaction at the Fe-TiN interface with first principles theory calculation, the Vienna ab initio Simulation Package (VASP) is adopted. PAW pseudopotentials with GGA-PBE functional are employed. Spin-polarized scheme is chosen to account for ferromagnetism of BCC-iron. The cut-off energy is 550eV due to the presence of helium. The TiN matrix can follow either the NaCl type lattice structure or TlI type lattice structure. The equilibrium energy per unit cell is -78.47eV for the NaCl type lattice and -76.20eV for the TlI type lattice. Meanwhile, we find that the TlI-type TiN is very sensitive to external perturbation. i.e., an interstitial He atom can lead to the TlI type lattice structure to transform into NaCl-type lattice structure due to the local lattice distortion. Therefore in our calculation, only NaCl-type lattice structure will be considered. Typically, there are 3 types of configurations for a binary interface: coherent interface, semi-coherent interface, and incoherent interface. At the coherent interface, two crystals match perfectly. The misfit in lattice parameter of two crystal lattice can be adjusted by small elastic strain. In the semi-coherent interface, two crystal lattices match in a periodic array. The lattice mismatch is not accommodated by long-term elastic strain, but by local lattice distortion. In the incoherent interface, the atoms are arranged in a disordered manner. Researchers are used to adopting coherent structures to perform the interface structure study with first principles theory calculations. It is because of its simplicity and low cost of computational effort, the typical lattice mismatch is within 10%. In a recent SEM experiment on BCC iron-TiC/N bonding interface, a semi-coherent structure is reported. Thus in our work, both coherent structure and semi-coherent structure are considered as shown in Fig. 6(c) and (d), respectively.

For both coherent configuration and semi-coherent configuration, the Fe atom at the iron slab has a choice to either facing one Ti atom or facing one N atom on the TiN slab. We calculate the interfacial energy γ_i for both possible configurations with the definition as shown below

$$2\gamma_i = E - N_{\mathrm{Fe}} \times E(\mathrm{Fe}) - N_{\mathrm{TiN}} \times E(\mathrm{TiN}), \quad (5)$$

where E is the total energy of the interface structure, E(Fe) and E(TiN) is the energy of Fe lattice and TiN lattice, N_{Fe} and N_{TiN} are the number of Fe atoms and TiN pairs in the interface structure. Our calculations show that γ_i is 3.73eV for Fe over N coordination and 5.81eV for Fe over Ti coordination. Thus we employ Fe over N coordination throughout the following study, as presented in Fig. 6(d).

In order to investigate the helium interaction with the Fe-TiN interface without influence from other interfaces, the slab thicknesses for Fe slab and TiN slab are important parameters that need to be determined. We calculate the energy of interface structure with different Fe slab thickness and TiN slab thickness for both the coherent configuration and semi-coherent configuration. We set the convergence criteria as the energy increment difference is less than 0.5% of the total energy. We also evaluate the interlayer distance between two layers of atoms within the slab. Therefore, in the following studies, we adopt a supercell containing 3 layers TiN slab and

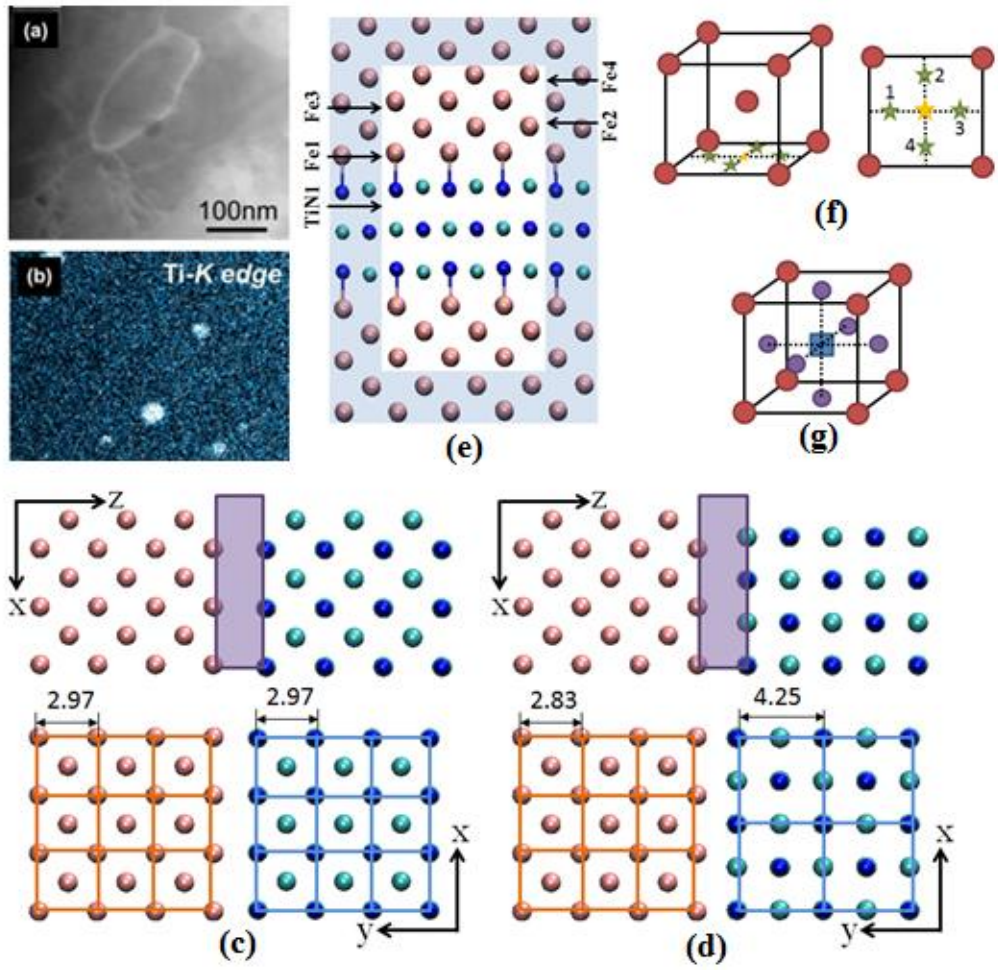

Figure 6: The lattice structure of Ti-rich nanoparticles in 14YWT (a) image from HAADF-STEM and (b) Ti chemical mapping with EDS. (c) schematic coherent interface structure. (d) schematic semi-coherent interface structure. Pink, blue and cyan spheres represent Fe, N and Ti atoms, respectively. The top figure shows the interface side view and the shaded area is the inter-facial region. The bottom figure shows the interface plane of two crystal, respectively. (x-y plane). The unit of lattice parameters shown in the figures is angstrom. (e-g) schematic representation of (e) The various locations (denoted as layer number) near the Fe-TiN interfacial region for the interstitial helium atoms, vacancy and O:Vac pair. (f) Interstitial sites for helium atom within the unit cell. The four tetrahedral sites are labeled with numbers. (g) The possible O:Vac pair orientations.

7 layers Fe slab as the coherent interface structure. Similarly, we decide to adopt a supercell containing 5 layers TiN slab and 13 layers Fe slab as the semi-coherent interface structure.

In order to understand the helium bubble nucleation and formation near the TiN nano-precipitants, we perform the energetic study about helium interaction with the Fe-TiN interface at various locations. As shown in Fig. 6(e), we consider 1 interstitial helium position within TiN lattice, denoted as TiN1 and 4 possible interstitial helium position within the Fe slab as Fe1, Fe2, Fe3, and Fe4. At each position, the interstitial helium can take the tetrahedral position and the octahedral position within the unit cell, as shown in Fig. 6(f). All 4 tetrahedral position are identical in this setup. Since the high oxygen solubility within 14YWT is due to the high density of pre-existing vacancy, it is necessary to take into account of such defects influence on the interaction between Fe-TiN interface and He atoms. Since it is difficult to form a vacancy in TiN lattice, we consider various types of interface structures with single point vacancy and O:Vac pair in the Fe slab and on the Fe-TiN interface, respectively. The O:Vac pair can have 6 different orientations within one BCC unit cell, as shown in Fig. 6(g). With the consideration of the periodic boundary condition and symmetricity of the interface lattice structure, all the possible sites for interstitial helium, vacancy and O:Vac pair will be considered.

In our calculation, the binding energy of helium is defined as

$$E_b(\mathrm{He}) = E(\mathrm{ref+He}) - E(\mathrm{ref}) - E(\mathrm{He}), \tag{6}$$

where E(ref) is the energy of the reference interface structure with He, E(ref +He) is the total energy of the interface structure with one interstitial He atom, and E(He) is the energy of one helium molecule. It has been proved that with the relaxed iron matrix, helium prefers to stay at the tetrahedral site with a lower formation energy. Helium prefers the tetrahedral site as well and it is easier for helium to be embedded into the iron matrix under the misfit strain. With a pre-existing vacancy, it is extremely easy for that vacancy to trap helium under the misfit strain condition, compared to the relaxed condition. With the oxygen pre-occupied at the vacancy site, it is still much easier for the O:Vac to trap helium under the misfit strain condition, compared to the relaxed condition.

Main Results

As shown in Fig. 6(e), we first investigate the binding energy variation of interstitial helium at the various site, including within TiN lattice, at Fe-TiN interface and within the Fe lattice near the interface. For each location, we consider one octahedral site and one tetrahedral site. The binding energy variation of the interstitial helium with respect to the locations are plotted in Fig. 7. Clearly, the binding energy of interstitial helium within TiN lattice is much higher than at the Fe-TiN interface and within the nearby iron lattice. At Fe4 location which is in the middle of Fe slab, the helium binding energy at the tetrahedral site is much lower than that at the octahedral site. It shows that the Fe-TiN interface has no influence on the Fe4 layer of the iron lattice, which means the iron slab thickness in this coherent interface structure is enough for us to investigate the Fe-TiN interface interaction with single helium atom. On the other hand, at the Fe-TiN interface or

near the Fe-TiN interface, the helium binding energy at the octahedral site is lower than that at the tetrahedral site. It means the Fe-TiN interface can affect the interstitial helium preference significantly. The binding energy of interstitial helium is not decreasing in a monotonic way when helium is moved from off inter-facial region to the near inter-facial region. When He is at the near inter-facial region (Fe1, Fe2), although there is extra space for Fe atoms to relax, the introduction of helium affects the Fe-N bonding, Ti-N bonding, and Fe-Ti repulsion. Therefore the overall energy is increasing. When He is in the off interfacial region (Fe4), the Fe-N and Ti-N bonding are not much affected but the Fe lattice distortion is significant. When He atom is at a tetrahedral interstitial site within Fe3 layer, the combining effect of Fe lattice distortion and bonding strength change at the interface reached an optimal value. In Table 2, the local Fe lattice distortion and the Ti-N bond length is shown to support the proceeding statement. The Fe-Fe bond distortion is more obvious with increasing layer number while the Ti-N bond distortion is diminishing.

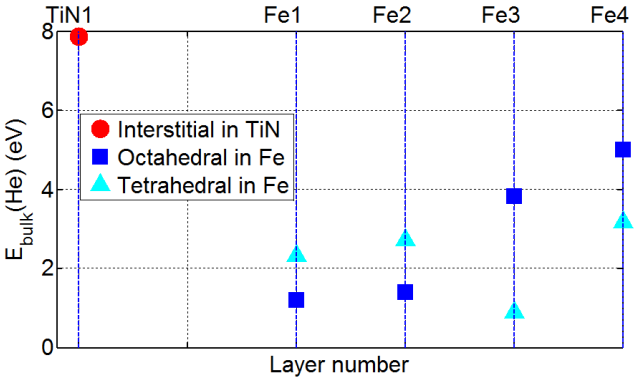

Figure 7. (a) The Charge distribution and (b) DOS of P_x orbital for neighboring Fe and N atoms at the coherent interface. The other two P orbitals show similar patterns thus not presented.

Bond type	Fe1	Fe2	Fe3	Fe4
Fe-Fe reference length	2.99	2.97	2.94	2.94
Fe-Fe bond	2.97	3.16	3.14	3.17
Fe-Fe bond	2.97	3.15	3.14	3.06
Fe-Fe bond	2.97	3.15	3.37	3.15
Fe-Fe bond	3.56	3.16	3.02	3.34
Elongation	4.3%	6.2%	7.7%	8.2%
Ti-N reference length	2.25	2.09	2.25	2.09
Ti-N bond	2.17	2.03	2.25	2.09
Elongation	-3.6%	-2.9%	0.0%	0.0%

Table 2. The local bond length variation near interstitial He in coherent interface. The four Fe-Fe bonds are the nearest Fe-Fe bonds to the interstitial He. The Ti-N bond is the nearest Ti-N bond to the interstitial He at the inter-facial region. The "Elongation" values denote the average percentage change from the reference bond length.

In this study, we consider the single point vacancy of iron atom both at the Fe-TiN interface and within the Fe slab. As shown in Fig. 6(e), four vacancy positions will be considered at the four layer of Fe atoms, shown as Fe1, Fe2, Fe3, and Fe4. From Fig. 8(a), we can clearly see that the helium atom can be easily trapped in the vacancy site at the TiN-Fe interface. One layer away from the TiN-Fe interface, the binding energy of helium with the vacancy in iron matrix remains stable. The helium atoms tend to take up the site of vacancies and act as a substitute of Fe atom in the interface, which implies vacancies are strong traps for helium atoms even with the excess space provided by the interfacial region. In other words, with the presence of vacancies, the entire interface structure shows homogeneity in attracting helium atoms. Due to the fact that the O:Vac pairs are pre-existing defects with high density in 14YWT. As is the case with the interface

structure with vacancies, the interface structure with O:Vac pairs also shows uniform affinity to helium atoms in the Fe slab as shown in Fig. 8(b). However, the binding energy between He and O:Vac E_b(He : (O : V ac))is much larger than in pure iron with coherency strain, which indicates a strong interaction occurs between O:Vac and the interfacial region when He enters the picture. With the local bond length variation analysis, the TiN-Fe interface has no influence on the helium interaction with O:Vac pair at Fe4 layer. Which means that the TiN-Fe interface will affect the helium interaction with iron matrix near the interface up to 4 layers of Fe atoms, regardless the existence of vacancy and vacancy pair.

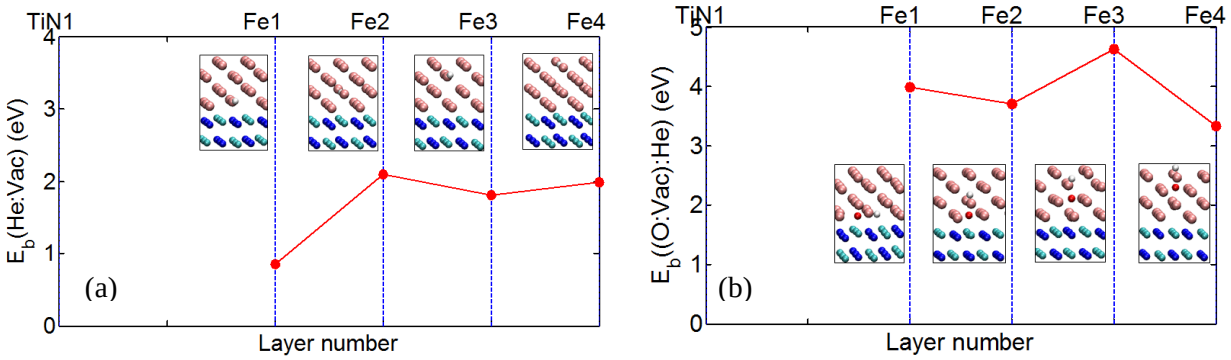

Figure 8: The helium binding energy variation with various vacancy positions (a) and O:Vac pair positions (b). The subfigures present the position of helium atoms (white ball) as a substitution in the lattice at each location.

Impact

We have performed first principles simulation about helium interaction at the TiN-Fe interface. A coherent interface structure and a semi-coherent interface structure are modeled. In both structures, The Fe over N coordination is determined to be energetically favorable. The Fe atom and N atom formed chemical bonding at the interfacial region. In the coherent interface, interstitial He atoms tend to be trapped in the interfacial region due to the excess space provided, despite the energy cost of altering the bonding status at the interface. The TiN-Fe interface will affect the preference site of interstitial helium within the iron matrix from the tetrahedral site to octahedral site. The TiN-Fe interface effects to the helium-iron interaction can be up to 4 iron layers. As shown in Fig. 8, at the TiN-Fe interface region (up to a 4th layer of Fe atoms), the helium binding energy is relatively smaller with the vacancy compared to the O:Vac pair. This research provided a fundamental understanding for future study of helium bubble interaction with TiN and other nanoparticles within 14YWT.

3.4 Strain Effects to the helium cluster behavior and elastic properties of 14YWT

Under real operating conditions, the structural components of nuclear reactors experience multiple types of external perturbation such as pressure, shear, moment, and thermal loadings. The structural materials undergo various strain states. Such external strain fields are known to greatly impact not only the mechanical properties of the material but also influence the gas atom (He) solution in the matrix. For instance, hydrostatic strain, which may be induced by gas bubble or

incompatibility between inclusion and matrix, greatly affects fracture behavior of materials and leads to early initiation of plasticity. It is also known to promote the brittle-ductile transition in BCC metals. Bi-axial stress also exists in structural components of nuclear systems. The ligament stress in the pressure vessel is usually considered as plane stress problem. Pre-existing strain can also affect the solution of gas atoms, such as helium and hydrogen, produced during irradiation, thus further influence the material performance. Experimentally, the elastic behavior of iron under pre-existing strain has been measured with ultra-sonic or diffraction techniques. An increase in the elastic constants is observed with increasing compressive loading. But no similar research has been conducted on 14YWT, where the matrix contains nanoclusters. Therefore, to provide full knowledge of 14YWT, it is necessary to study the gas atom solution in 14YWT under pre-existing strain. In addition to the NC units, the iron matrix can contain other defects as vacancies. Hence, the study of the defected iron matrix is also of great significance. In this work, various local atomic environments in 14YWT under pre-existing strain will be investigated with density functional theory calculation. The local atomic configurations include typical NC unit and common defects in 14YWT. To elucidate the effect of pre-existing strain on the solution of helium in 14YWT, an energetic study of helium formation energy is performed.

Approaches and models

In the investigation of helium energetic behavior and elastic constants evolution in 14YWT under pre-existing strain, we adopted the Vienna *ab initio* simulation package (VASP) to perform density functional theory calculations. To describe the ferromagnetism of α-iron, spin-polarized scheme is switched on. The electron-ionic core interaction is interpreted with PAW pseudopotential. The exchange and correction relation of electrons is described with GGA\PBE functionals. A cut-off energy is set to 480eV in the calculation. We construct a supercell consisting of 4×4×4 unit cells (128 Fe atoms with the perfect lattice) as the simulation domain for all the energetic studies during the calculations. A 3×3×3 k-mesh is generated by applying the Monkhorst-Pack method.

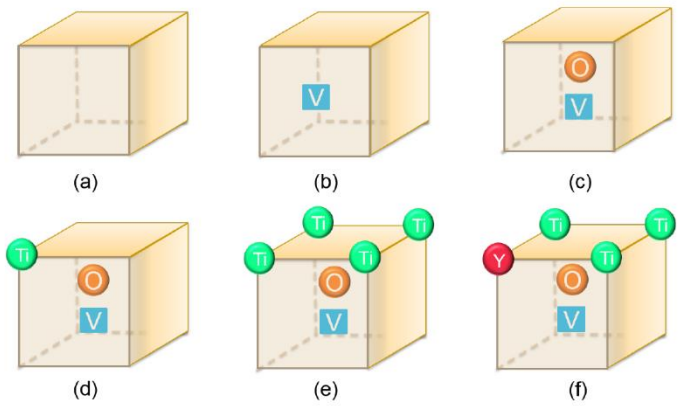

Figure 9: (a)-(f) Schematic atomic configuration of the BCC reference units. (a) pure Fe lattice, (b) Fe+Vac, (c) Fe+O:Vac, (d) Fe+O:Vac+1Ti, (e) Fe+O:Vac+4Ti, (f) Fe+O:Vac +3Ti+Y, Fe atoms are on the lattice sites for the BCC unit unless otherwise marked with symbols with solute atoms

In this work, six typical reference units in Fe matrix are selected to study the helium behavior under pre-existing strain within 14YWT matrix, which is shown in Fig. 9. The helium atom will be placed in the pure iron lattice as shown in Fig.9 (a). In Fig.9 (b), helium atom will be

interacting with a vacancy, which is a common defect in the iron matrix, especially under irradiation. A unit cell with O:Vac pair is depicted in Fig.9 (c). Fig.9 (d-e) show the typical atomic structures of Y-Ti-O enriched nano-clusters in 14YWT. Each of the units is embedded with an O:Vac pair in the center. The neighboring Fe atoms may be substitute with Ti or Y solute atoms. In each of the 6 cases in our calculation, the reference unit will be placed in the center of the supercell. In other words, one of the 128 Fe cells is replaced by the reference unit, while the rest 127 cells remain to be BCC Fe cells to simulate Fe matrix around NC. For each of the six reference configurations, two types of strains are applied to the simulation domain, respectively. Namely, the hydrostatic tri-axial strain and in-plane bi-axial strain are considered. These two types of strains are common in structural materials of nuclear systems under operation. In addition, hydrostatic strain preserves the symmetry of the lattice, while bi-axial strain breaks the lattice symmetry. Thus the study of such 2 types of strains can produce representative results on 14YWT response to external strain field. The strain ranges from 2% compressive strain to 2% tensile strain, which is of the similar magnitude of lattice strain observed in previous experimental studies on mechanical deformation of iron-based NFAs. In this study, all the results are obtained with the fixed volume scheme. The strain-free lattice constant of the BCC iron matrix is a_0=2.83Å. We adopted the concept of formation energy to investigate the affinity of helium to the reference. The formation energy of helium is defined as

$$E_f\,(\text{ref+He}) = E(\text{ref+He}) - E(\text{ref}) - E(\text{He}), \tag{7}$$

where ref + He presents the system where a helium atom is located near the reference unit in the super-cell. Subscript f stands for the formation energy. E(He) denotes the energy of an isolated helium atom in a vacuum, which is negligible as the value is almost zero in our work. In order to investigate the interaction of helium with a certain type of trapping site, the binding energy between helium and the trapping site is computed. If the interaction is to be attraction, the binding energy is negative, which is defined as

$$E_{bind}(\text{ref+He}) = E_f(\text{ref+ He}) - E_f\,(\text{ref+ He}) - E_f\,(\text{He}_{tetra}), \tag{8}$$

where $E_f\,(\text{He}_{tetra})$ is the formation energy of an interstitial helium atom at the tetrahedral site in the perfect Fe lattice since helium requires the lowest energy at this position.

The various pre-strain conditions are applied to the calculation domain by controlling the volume. The strain-free lattice constant of the BCC iron matrix is defined as a_0 = 2.83Å. In order to calculate the strain effect to the elastic constants within 14YWT, manual lattice distortion is applied to the reference super cell configuration. For BCC structures, there are three independent elastic constants, namely, C_{11}, C_{12}, and C_{44}. To obtain these three elastic constants, we first calculate the strain-energy coefficients C'_{11}, C'_{12}, and C'_{44}. When loaded with a Cauchy strain tensor $\boldsymbol{\varepsilon}$ as,

$$\varepsilon_1 = \begin{Bmatrix} \delta & 0 & 0 \\ 0 & \delta & 0 \\ 0 & 0 & \delta \end{Bmatrix}, \qquad \varepsilon_2 = \begin{Bmatrix} \delta & 0 & 0 \\ 0 & -\delta & 0 \\ 0 & 0 & \dfrac{\delta^2}{\left(1-\delta^2\right)} \end{Bmatrix}, \qquad \varepsilon_1 = \begin{Bmatrix} 0 & \dfrac{\delta}{2} & 0 \\ \dfrac{\delta}{2} & 0 & 0 \\ 0 & 0 & \dfrac{\delta^2}{4-\delta^2} \end{Bmatrix}, \tag{9}$$

where δ is a small value of strain. The energy of the current distorted configuration for each strain status can then be written as,

$$E\left(p_{ij},\varepsilon\right) = \begin{cases} E\left(p_{ij},0\right) + \dfrac{3}{2}\left(C'_{11} + 2C'_{12}\right)V\delta^2 + O\left(\delta^3\right) & if \quad \varepsilon = \varepsilon_1 \\ E\left(p_{ij},0\right) + \left(C'_{11} - C'_{12} - P\right)V\delta^2 + O\left(\delta^4\right) & if \quad \varepsilon = \varepsilon_2 \\ E\left(p_{ij},0\right) + \dfrac{1}{2}\left(C'_{44} - \dfrac{P}{2}\right)V\delta^2 + O\left(\delta^4\right) & if \quad \varepsilon = \varepsilon_3 \end{cases} \tag{10}$$

where $E(p_{ij}, \varepsilon)$ is the current energy with strain ε and hydrostatic stress $p_{ij} = -P\delta_{ij}$, $E(p_{ij}, 0)$ is the energy of the calculation domain under pre-existing stress p_{ij} (pressure P), and V is the volume of the system. By applying a series of δ ranging within ±3.5% for C'_{11}, C'_{12}, and ±4.5% for C'_{44}, the strain-energy coefficients can be obtained from quadratic fitting of the energy. Since it is more practical to use stress-strain coefficients instead of strain-energy coefficients in engineering, the stress-strain coefficients will be determined. The calculated strain-energy coefficients C'_{11}, C'_{12} and C'_{44} satisfy the following relations with the elastic constants C_{11}, C_{12} and C_{44} [j],

$$C_{11} = C'_{11} \qquad C_{12} = C'_{12} + P \qquad C_{44} = C'_{44} - \frac{P}{2} \tag{11}$$

From the calculated elastic constants, the polycrystalline elastic parameters such as Young's modulus E, Poisson's ν, bulk modulus B and shear modulus G of the reference structures can be obtained with polycrystalline theories.

For the structures under bi-axial strain, the BCC iron lattice transformed into a BCT (body-centered tetragonal) lattice. The independent elastic constants then consist of C_{11}, C_{12}, C_{13}, C_{33}, C_{44}, and C_{66}. Thus another 3 sets of strains in addition to strains in Eq.(9) will be applied to obtain the elastic constants for structures under bi-axial strain.

[j] T. H. K. Barron and M. L. Klein, "Second-order elastic constants of a solid under stress", Proceedings of the Physical Society, vol: 85(3), pp: 523, 1965

$$\varepsilon_4=\begin{Bmatrix}0&0&0\\0&0&0\\0&0&\delta\end{Bmatrix},\qquad \varepsilon_5=\begin{Bmatrix}\delta&0&0\\0&\dfrac{\delta^2}{\left(1-\delta^2\right)}&0\\0&0&-\delta\end{Bmatrix},\qquad \varepsilon_6=\begin{Bmatrix}0&0&\dfrac{\delta}{2}\\0&\dfrac{\delta^2}{4-\delta^2}&0\\\dfrac{\delta}{2}&0&0\end{Bmatrix}, \tag{12}$$

Note that the initial stress state of a BCT structure under bi-axial strain in x-y plane can be written as $p_{ij} = -P\delta_{ij} + Q_{ij}$. Q_{ij} is only non-trivial if $i = j = 3$. Therefore, the energy of the BCC lattice under bi-axial in-plane stress p_{ij} can be defined as,

$$E\left(p_{ij},\varepsilon\right)=\begin{cases}E\left(p_{ij},0\right)+\dfrac{1}{2}\left(2C'_{11}+C'_{33}+4C'_{12}+2C'_{13}\right)V\delta^2+O\left(\delta^3\right) & if \quad \varepsilon=\varepsilon_1\\ E\left(p_{ij},0\right)+\left(C'_{11}-C'_{12}-P+Q_{33}\right)V\delta^2+O\left(\delta^4\right) & if \quad \varepsilon=\varepsilon_2\\ E\left(p_{ij},0\right)+\dfrac{1}{2}\left(C'_{66}-\dfrac{P}{2}+\dfrac{Q_{33}}{2}\right)V\delta^2+O\left(\delta^4\right) & if \quad \varepsilon=\varepsilon_3\\ E\left(p_{ij},0\right)+\dfrac{1}{2}\left(C'_{33}\right)V\delta^2+O\left(\delta^3\right) & if \quad \varepsilon=\varepsilon_4\\ E\left(p_{ij},0\right)+\dfrac{1}{2}\left(C'_{11}+C'_{33}-2C'_{13}-2P\right)V\delta^2+O\left(\delta^3\right) & if \quad \varepsilon=\varepsilon_5\\ E\left(p_{ij},0\right)+\dfrac{1}{2}\left(C'_{44}-\dfrac{P}{2}\right)V\delta^2+O\left(\delta^4\right) & if \quad \varepsilon=\varepsilon_6\end{cases} \tag{13}$$

The relation between the strain-energy coefficients C'_{ij} and the elastic constants C_{ij} is,

$$\begin{aligned}&C_{11}=C'_{11}\quad C_{33}=C'_{33}\quad C_{12}=C'_{12}+P\\ &C_{13}=C'_{13}+P-\frac{Q_{33}}{2}\quad C_{44}=C'_{44}-\frac{P}{2}+\frac{Q_{33}}{4}\quad C_{66}=C'_{66}-\frac{P}{2}\end{aligned} \tag{14}$$

Results and discussion

In defect free matrix, helium atom tends to occupy tetrahedral sites despite of pre-existing strains. As the strain turns from compressive to tensile, the formation energy of helium continues to drop under both types of strain, where hydrostatic strain gives a steeper slope of formation energy curve. The formation energy maintains higher under bi-axial strain than under hydrostatic strain. Helium atoms prefer tetrahedral sites under both hydrostatic and bi-axial strain. With the introduction of vacancy, helium atom tends to take up the empty site and behaves as a substitution atom. The large reduction in the formation energy implies that vacancies exert strong attraction to helium atoms, comparing to the vacancy free case. The O:Vac pair also shows strong affinity to helium in all strained cases, but with a slightly higher formation energy. In these two reference configurations, the formation energy for helium also reduces with increasing tensile strain, regardless of the strain type (hydrostatic or bi-axial). But different from the pure Fe lattice

configuration, in the defected lattice, helium formation energy, though slightly, is lower in bi-axial strain cases than in hydrostatic strain cases. Such difference gradually vanishes and can eventually experience a reverse, which indicates the excess space produced by vacancy is especially advantageous for the absorption of helium under bi-axial compression. While with the increasing of strain, expansion of cell volume starts to take effect on helium formation energy. The formation energy sees a steeper decrease under hydrostatic strain than under bi-axial strain in Fe+Vac and Fe+O:Vac lattices.

With the solute atom Ti taking up the atomic position of Fe, which is typical in nano-cluster units, helium atom still tends to be attracted to the vacancy in the O:Vac pair. Similar to the Fe+O:Vac lattice, the formation energy of helium in both lattices is decreasing with the increase of strain. The decreasing also showed a slightly steeper trend under hydrostatic strain than under bi-axial strain in both lattices. The solute atom Ti has repulsion effect on the helium atom as we have observed in our previous study. With the number of Ti atoms increasing from one to four, an increase of 0.1eV is observed in the helium formation energy under same strain status.

To understand the mechanism of such helium formation energy variation in reference lattices under pre-existing strain. The local lattice distortion near helium atom, as well as the binding energy of helium with trapping sites, are investigated. In Fig. 10, the bond strain, i.e., the relative elongation of bonds in the reference unit containing helium is presented. The bonds of interest are marked as *a*, *b*, and *c* in Fig. 11. In all cases under hydrostatic strain, a clear increasing trend of bond strain in *a* and *b* type bonds can be observed. The bond strain in *c* type bonds either increases or stay nearly unchanged. Such results indicate that with the increase of strain, helium experiences less impedance to distort the cell and expand the cell volume. In other words, with larger pre-existing strain, there is more atomic space in the iron matrix for helium atoms to be fitted into, thus causing the reduced energy cost of capturing helium. The smoother slope in the compressive region and steeper slope in the tensile region are also in correspondence to slower and faster formation energy reduction in the two strain ranges. In cases under bi-

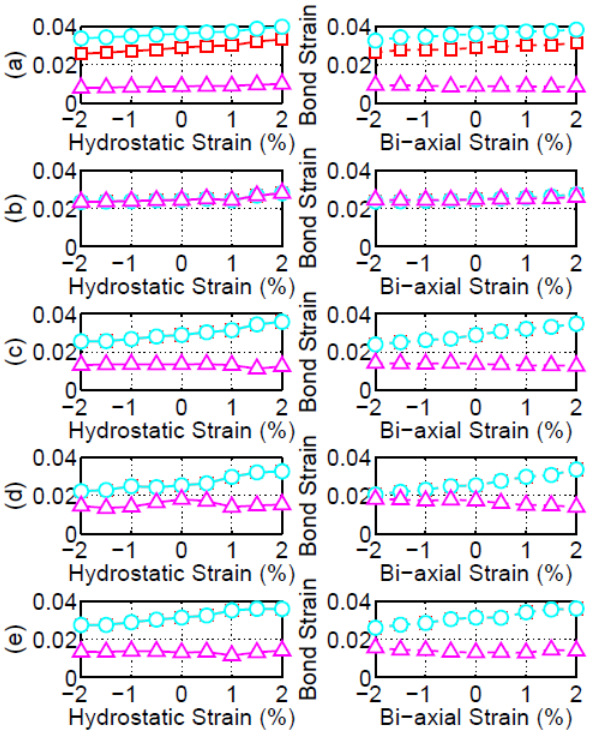

Figure 10: The lattice distortion of the unit cell containing helium atom in four reference lattices. (a) Fe lattice, (b) Fe+Vac lattice (c) Fe+O:Vac lattice, (d) Fe+O:Vac+1Ti lattice, and (e) Fe+O:Vac+4Ti. The red, blue and magenta symbols represent average bond strain in *a*, *b*, and *c* directions, respectively. The *a*, *b*, and *c* directions are shown in Fig.11.

axial strain, the variations of bond strain are similar in Fe+Vac, Fe+O:Vac, and Fe+O:Vac+1Ti to their hydrostatic counterparts. But the bond variation is different in pure Fe lattice. In this case, *a* and *b* types bonds, which are under bi-axial strain, barely change. Only *c* type bonds, which are those along the out of plane direction of the bi-axial strain field, experience relaxation.

Such behavior of helium under pre-existing strain in 14YWT leads to another reason why nano-clusters and nano-precipitates can attract helium bubbles. In typical NC unit, the O:Vac induces local tensile strain field near to the vacancy side. While O atom in O:Vac pair, Solute atom Ti and Y induce local compression, a helium atom is more likely to be trapped to the vacancy side of O:Vac pair both due to the existence of a vacancy and the surrounding tensile strain. At the same time, due to the compressive strain field produced by O and other solute atoms, helium atoms are less likely to accumulate or migrate to those directions as shown in Fig.11. Thus nano-clusters can influence the formation and distribution of helium bubbles not only via chemical interaction of helium with O:Vac, Ti, and Y, but also via strain field near NCs. The same mechanism can apply to the matrix-NP interface where pre-existing lattice distortion is presented. Moreover, these results also outline the affinity of helium to structural steel which is already in operation and has experienced various pressure states.

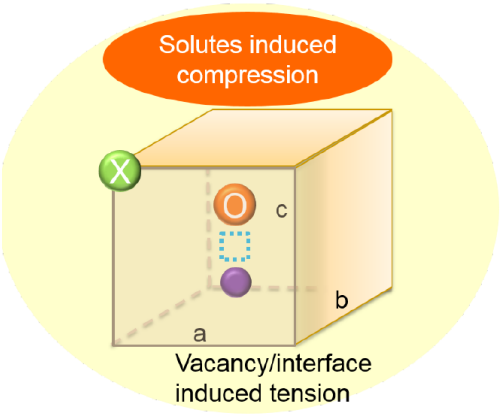

Figure 11: Schematic of the unit cell containing helium atom. The helium atom is denoted by the purple sphere. The blue dashed square denotes the vacancy. Green "X" denotes possible solute atom (Ti, Y). The bonds in 3 Cartesian directions are denoted as *a*, *b*, and *c*

Besides the effect of pre-existing strain on lattice distortion, the effect on interaction between helium and major trapping sites are also studied. The binding energy between helium/Vac or helium/O:Vac is summarized in Fig.12. It is noticed that the binding energies grow with increasing hydrostatic strain, denoting a weaker attraction between helium and trapping sites. The reduction of helium formation energy relies more and more on the lattice relaxation. While in bi-axial strain cases, the binding energies first increase with strain in compressive range, then reduce with strain in tensile range. Such flip over indicates the un-relaxed out of plane direction in the bi-axial strain tests can greatly affect the interaction of helium with trapping sites. Closer inspection on the helium-oxygen atomic distance, as shown in Fig.13, demonstrates that He-O distance increases faster under hydrostatic strain than under bi-axial strain, which means that the impact O atom and He atom on each other are decaying faster in under hydrostatic strain.

We further investigated the impact of pre-existing strains on the elastic properties of 14YWT. The elastic constants of Fe lattice of 14YWT with various initial local states are calculated. The existence of compressive strain hardens the Fe matrix while the tensile strain softens the Fe matrix, regardless of initial strain type. The hydrostatic strain, however, alters the

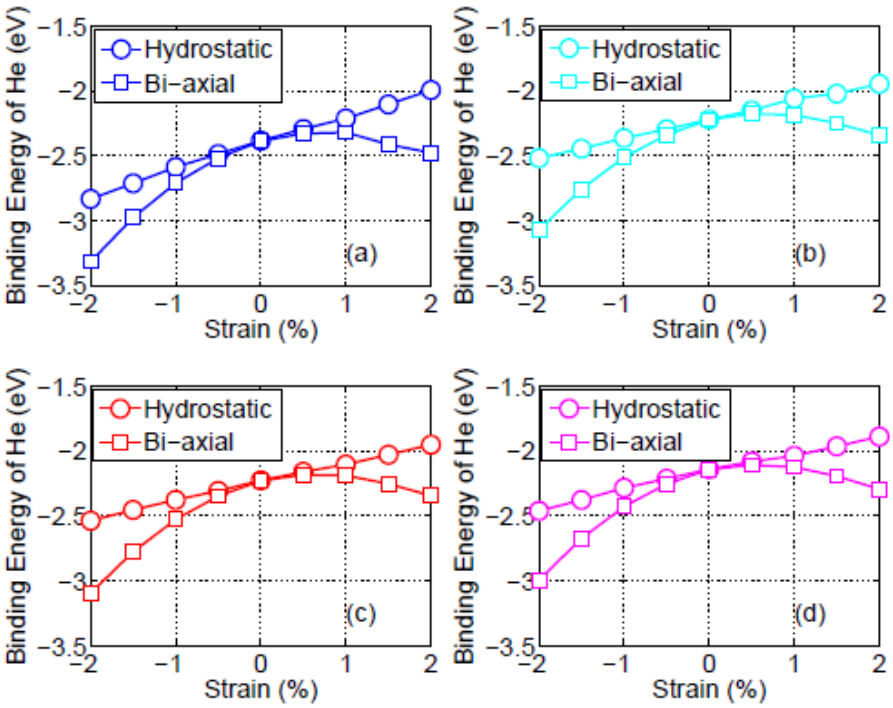

Figure 12: The binding energy of helium atom in four reference lattices. (a) helium impurity atom attracted to vacancy in Fe+Vac lattice, (b) helium impurity atom attracted to vacancy in Fe+O:Vac lattice (c) helium impurity atom attracted to vacancy in Fe+O:Vac+1Ti lattice, and (d) helium impurity atom attracted to vacancy in Fe+O:Vac+4Ti lattice

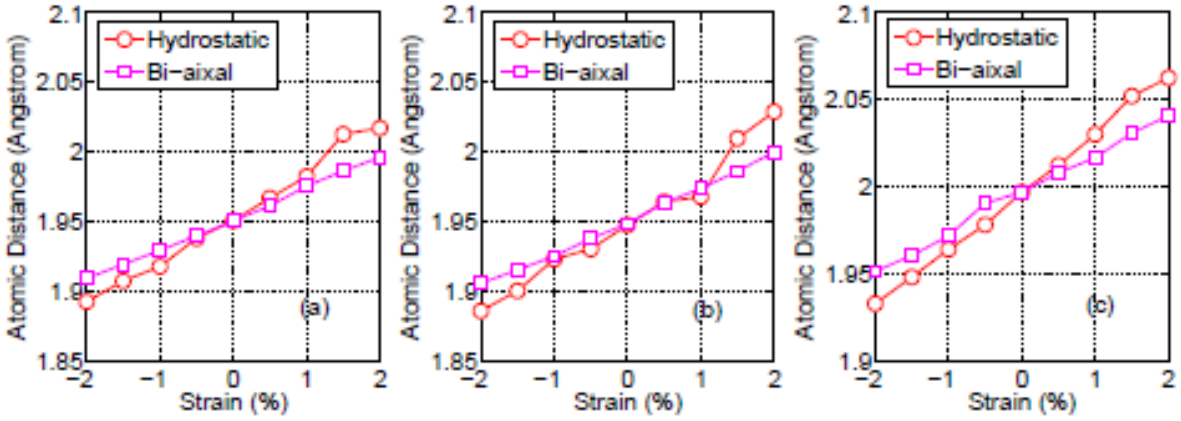

Figure 13: The O-He distance in two reference lattices. (a) Fe+O:Vac lattice, (b) Fe+O:Vac+1Ti lattice, and (c) Fe+O:Vac+4Ti lattice

values of elastic constants in a more drastic manner, comparing to bi-axial strain with the same magnitude. The introduction of bi-axial initial strain breaks the symmetry of the BCC Fe lattice, resulting in the splitting between C_{11}/C_{22} and C_{33}. The former varies more gently with a change in strain magnitude. There are also differences between C_{12} and C_{13}, C_{44} and C_{66}. But the difference is relatively small, in the following of the discussion, only the difference between C_{11} and C_{33} will

be presented to illustrate the effect of broken symmetry for structures under pre-existing bi-axial strain. In the deformed Fe lattice under bi-axial strain, C_{11} is varying with larger slope than C_{33} due to the larger magnitude of in-plane distortion than the out-of-plane distortion. The split of C_{11} and C_{33} also indicates a greater extent of elastic anisotropy in Fe lattice under bi-axial pre-existing strain.

The Young′s modulus in various crystallographic orientations of the deformed Fe lattice are calculated for a more detailed study on elastic anisotropy. It is well known that single crystal Fe lattice should display different elastic behaviors in different directions, due to the difference of atomic packing in various crystallographic orientations. The Young′s modulus in a certain orientation can be determined with Voigt-Reuss-Hill theory[k,l]. The equations (15)

$$\begin{cases} E_{hkl:hydro} = \dfrac{1}{\left(S_{11}-2\left(S_{11}-S_{12}\right)-S_{44}/2\right)\left(l_1^2l_2^2+l_2^2l_3^2+l_1^2l_3^2\right)} \\ E_{hkl:biaxial} = \dfrac{1}{S_{11}\left(l_1^4+l_2^4\right)+\left(2S_{13}+S_{44}\right)\left(l_2^2l_3^2+l_1^2l_3^2\right)+S_{33}l_3^4+\left(2S_{12}+S_{66}\right)l_1^2l_2^2} \end{cases} \quad (15)$$

render Young's modulus in (*hkl*) crystallographic orientation in Fe lattice under hydrostatic strain (cubic structure) and bi-axial strain (tetragonal structure), respectively. In Eq.(15), E_{hkl} stands for Young's modulus in orientation (*hkl*). The subscripts hydro and biaxial denote the type of pre-existing strain. S_{ij} is the elastic compliance. l_1, l_2, and l_3 are the directional cosines of direction (*hkl*). The orientation dependence of Young's modulus in pure Fe is presented in Fig. 14 at an extreme pre-existing tensile strain of 2%. As indicated by the split in C_{11} and C_{33}, it is clear that

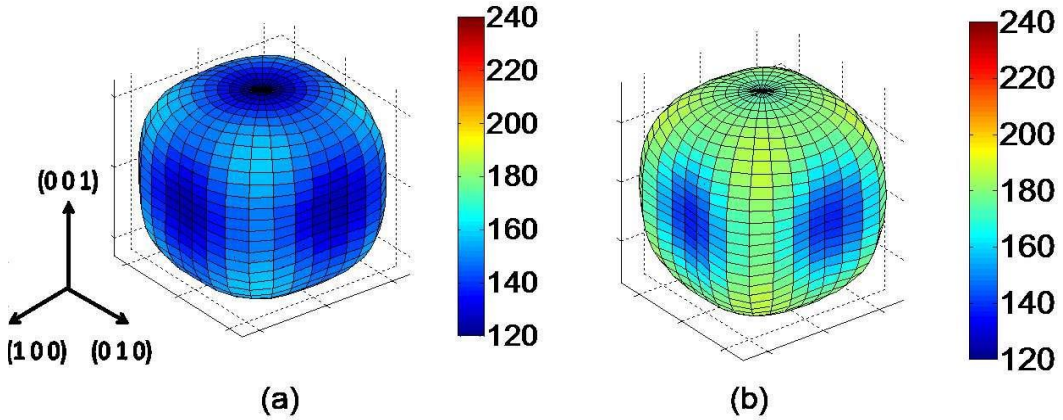

Figure 14. Young's modulus variation in pure Fe lattice under 2% (a) hydrostatic, and (b) bi-axial tensile strain. Unit: GPa

[k] R. Hill, "The elastic behaviour of a crystalline aggregate", Proceedings of the Physical Society Section A, vol: 65(5), pp:349, 1952

[l] J. Feng, B. Xiao, R. Zhou, W. Pan, and D. R. Clarke, "Anisotropic elastic and thermal properties of the double perovskite slabrock salt layer $Ln_2SrAl_2O_7$ (Ln= La, Nd, Sm, Eu, Gd or Dy) natural superlattice structure", Acta Materialia, vol: 60(8), pp: 3380-3392, 2012

the anisotropy is more obvious in structures under initial bi-axial strain. In all cases tested under initial strain, the elastic hardest direction is the closest packed (111) direction as shown in Fig.14.

Under hydrostatic pre-existing strain, Fe lattice shows smallest Young's modulus in (001) (equivalent to (100) and (010)). When placed under bi-axial pre-existing strain, the elastic softest direction gradually shifts from (001) direction to (100) direction, from compressive strain to tensile strain. The evolution of elastic anisotropy with the magnitude of pre-existing strain is investigated via the calculation of anisotropy parameters. These parameters are defined in Eq.(16) and Eq.(17) for hydrostatic strain and bi-axial strain, respectively[m].

$$A_0 = \frac{(2C_{44})}{(C_{11} - C_{12})} \tag{16}$$

$$\begin{cases} A_1 = \dfrac{4C_{44}}{(C_{11} + C_{33} - 2C_{13})} \\ A_2 = \dfrac{2C_{66}}{(C_{11} - C_{12})} \end{cases} \tag{17}$$

In Eq.(16), A_0 is the anisotropy parameter for structures under hydrostatic strain. In Eq.(17), A_1 and A_2 are the anisotropy parameters for structures under bi-axial strain, where A_1 denotes the out-of-plane anisotropy and A_2 denotes the in-plane anisotropy. The calculated anisotropy elastic constants are shown in Fig. 15. In the case where hydrostatic pre-existing strain is presented, the elastic anisotropy is weakening from compressive strain range to tensile strain range. The A_1 parameter also shows a weakening elastic anisotropy in structures under pre-existing bi-axial strain. However, the A_2 parameter barely changes. The different behaviors of A_1 and A_2 indicate that in the structures under bi-axial strain, the out-of-plane anisotropy is much more affected by the pre-existing strain than the in-plane anisotropy.

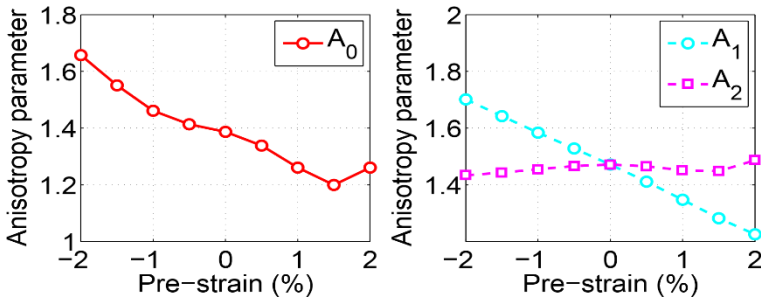

Figure 15. Anisotropy parameters variation in pure Fe lattice under (a) hydrostatic, and (b) bi-axial pre-existing strain

The elastic anisotropy plays an important role in the deformation of polycrystalline materials, such as the activation of slip planes. It also influences fabrication and texture (preferred

[m] B. Xiao, J. Feng, C. T. Zhou, Y. H. Jiang, and R. Zhou, "Mechanical properties and chemical bonding characteristics of Cr_7C_3 type multicomponent carbides", Journal of Applied Physics, vol: 109(2), pp: 023507, 2011

orientation) of materials under rolling conditions. In the following, the effect of elastic anisotropy on favorable slipping directions in Fe lattice under hydrostatic preexisting strain is investigated. The key slipping planes are usually closed packed planes such as {110} and {112} in BCC materials. The favorable slipping directions are the directions with smallest shear modulus on these planes. We calculated the orientation dependent shear modulus (G_{23}) of Fe lattice under various pre-existing strains according to the method described in Ref[n]. The results are shown in Fig. 16. Each curve in the figure represents the shear modulus variation with directions in a slipping plane under a specific pre-existing hydrostatic strain. The distance between a point on the curve and the origin stands for the magnitude of the shear modulus. The results show that with the pre-existing strain varying from tensile strain to compressive strain, the shear moduli in all directions experience an increase. But the speed of the increment is not the same for different orientations, implying a pronounced elastic anisotropy, which is in accordance with the results shown in Fig. 16. On both key slipping planes, the shear modulus is the smallest in (111) direction under all magnitudes of pre-existing strain. Therefore, the favorable direction of slipping will always be (111) regardless of strain. The tendency of the slipping happening in (111) is becoming more obvious with pre-existing strain turning from tensile strain to compressive strain.

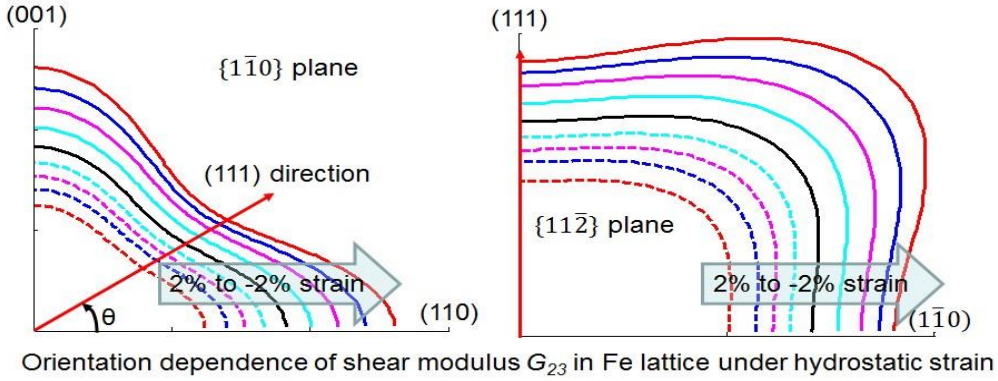

Figure 16. Orientation dependence of shear modulus G_{23} on two key slipping planes in Fe lattice under hydrostatic strain

Due to the fact that it is highly unlikely that the 14YWT can be prepared in single crystal form, it is necessary to study the polycrystalline properties of 14YWT, which is more of engineering significance. The polycrystalline elastic parameters are calculated according to the Voigt-Reuss-Hill approximation[o,p]. The polycrystalline 14YWT is treated as an isotropic material where its elastic properties can be characterized by any two of the following parameters: Young's

[n] J. Turley and G. Sines, "The anisotropy of Young's modulus, shear modulus and Poisson's ratio in cubic materials", Journal of Physics D: Applied Physics, vol: 4(2), pp:264, 1971

[o] R. Hill, "The elastic behaviour of a crystalline aggregate", Proceedings of the Physical Society Section A, vol: 65(5), pp:349, 1952

[p] J. Feng, B. Xiao, R. Zhou, W. Pan, and D. R. Clarke, "Anisotropic elastic and thermal properties of the double perovskite slabrock salt layer $Ln_2SrAl_2O_7$ (Ln= La, Nd, Sm, Eu, Gd or Dy) natural superlattice structure", Acta Materialia, vol: 60(8), pp: 3380-3392, 2012

modulus E, Bulk modulus B, shear modulus G and Poisson's ratio ν. These parameters can be obtained by methods described in Ref[l,q],

$$\begin{cases} B = \frac{1}{2}\left(B_V + B_R\right) & G = \frac{1}{2}\left(G_V + G_R\right) \\ E = \frac{9BG}{3B+G} & \nu = \frac{3B-2G}{6B+2G} \end{cases} \tag{18}$$

where the subscripts V and R stand for the elastic parameters obtained from the Voigt and Reuss models, respectively. B_V, B_R, G_V, and G_R can be calculated from the single crystal elastic constants according to the following equations[j], Note that in the case of hydrostatic pre-existing strain, $C_{11} = C_{33}$, $C_{13} = C_{23}$, and $C_{44} = C_{66}$.

$$\begin{cases} B_V = \frac{1}{9}\left(2\left(C_{11}+C_{12}\right)+C_{33}+4C_{13}\right) & B_R = \frac{C^2}{M} \\ G_V = \frac{1}{30}\left(M+3C_{11}-3C_{12}+12C_{44}+6C_{66}\right) & G_R = \frac{15}{\frac{18B_V}{C^2}+\frac{6}{C_{11}-C_{12}}+\frac{6}{C_{44}}+\frac{3}{C_{66}}} \\ M = C_{11}+C_{12}+2C_{33}-4C_{13} & C^2 = \left(C_{11}+C_{12}\right)C_{33}-2C_{13}^2 \end{cases} \tag{19}$$

In Fig. 17, the polycrystalline Young's modulus and shear modulus variation with pre-existing strain is presented. Similar to the single crystal elastic constants, both elastic moduli are decreasing almost linearly with reducing compressive strain and increasing tensile strain, which denotes that, with the grain-grain interaction taken into account, the preexisting tensile strain can have softening effect on aggregation of iron grains. The decrease in elastic moduli shows a steeper trend in the hydrostatic case than that in the bi-axial case, which is reasonable due to a more severe degree of deformation in the Fe lattice under hydrostatic pre-existing strain.

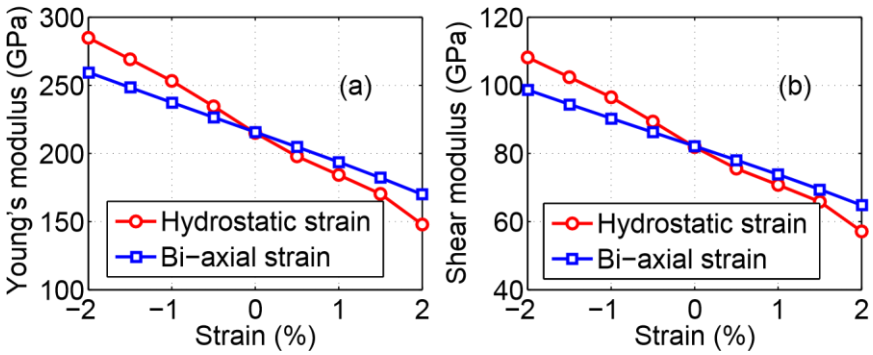

Figure 17. Polycrystalline elastic parameters (a) Young's modulus, and (b) shear modulus variation in pure Fe lattice under hydrostatic strain and bi-axial strain

[q] M. A. Hopcroft, W. D. Nix, and T. W. Kenny, "What is the Young's Modulus of Silicon?", Journal of microelectromechanical systems, vol: 19(2), pp: 229-238, 2010

The effect of the helium atom can be a combination of matrix hardening via generation of compressive strain on the surrounding Fe matrix, and a local softening via local atomic interaction. To investigate both influences of helium on the surrounding matrix, the variation of elastic constants of the entire structure and the Fe matrix alone is calculated. The variation of elastic constants of the entire structure is defined as $(C^{total}_{11}(X+He)-C^{total}_{11}(X))/C^{total}_{11}(X)$. The superscript total denotes that the C_{11} value is for the entire structure illustrated in the top row of the schematic shown in Fig. 18. The superscript matrix represents that the C_{11} is for the Fe matrix alone in the structure as shown in the bottom row in Fig. 10. In this case, C_{11} is only calculated for the Fe matrix surrounding the unit cell containing the helium atom. The unit cell containing the helium is not considered.

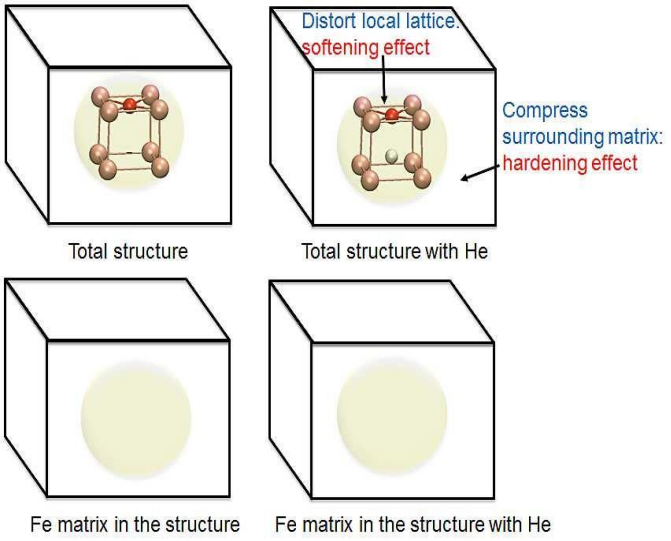

Figure 18. Schematic of the entire structure and the Fe matrix in the structure

The matrix values for elastic constants of the Fe matrix in a certain structure are obtained by plugging the stress of that structure into the Murnaghan equation. The Murnaghan equation provides a linear relationship between the current hydrostatic stress and elastic constants[r]. In our calculation, the hydrostatic stress takes the unit of GPa. Eq.(20) gives the form of Murnaghan equation in our calculation.

$$\begin{cases} C_{11} = ca_1 \times \sigma_{hydro} + ca_2 \\ C_{12} = cb_1 \times \sigma_{hydro} + cb_2 \\ C_{44} = cc_1 \times \sigma_{hydro} + cc_2 \end{cases} \quad (20)$$

In this equation, σ_{hydro} is the hydrostatic stress of current structure. ca_1, ca_2, cb_1, cb_2, cc_1, and cc_2 are coefficients that are obtained by linear fitting of elastic constants and corresponding hydrostatic stress for the pure Fe lattice. The values of these parameters are listed in Table 3. For a certain structure under hydrostatic strain, the term σ_{hydro} in Eq.(20) can be evaluated with the hydrostatic stress which is experienced by that structure. The corresponding coefficients ca_1, ca_2,

[r] H. B. Zhou, S. Jin, Y. Zhang, G. H. Lu, and F. Liu, "Anisotropic strain enhanced hydrogen solubility in bcc metals: the independence on the sign of strain", Physical review letters, vol:109(13), pp:135502, 2012

cb_1, cb_2, cc_1, and cc_2 are then plugged into the equation to calculate regarding elastic constants for the Fe matrix.

Table 3. The coefficients in Murnaghan equation

ca_1(1)	ca_2 (GPa)	cb_1(1)	cb_2 (GPa)	cc_1(1)	cc_2 (GPa)
8.04±0.21	260.90±6.17	5.11±0.03	137.60±3.47	2.91±0.04	89.69±0.61

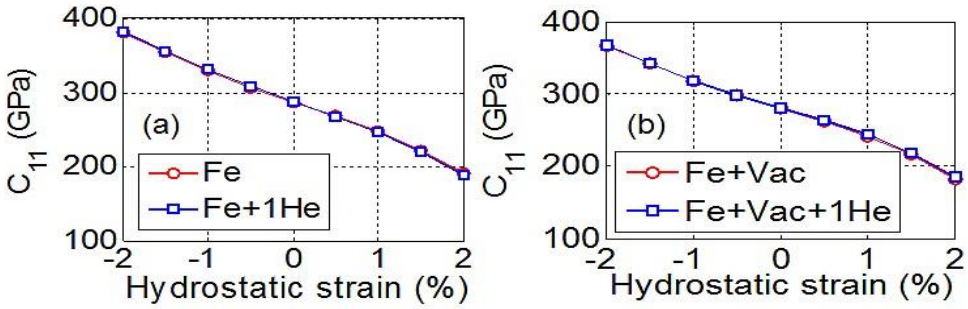

Figure 19. Elastic constant C_{11} evolution in pure Fe under hydrostatic strain. (a) C_{11} in Fe lattice and Fe+1He lattice (b) C_{11} in Fe+Vac and Fe+Vac+1He structure

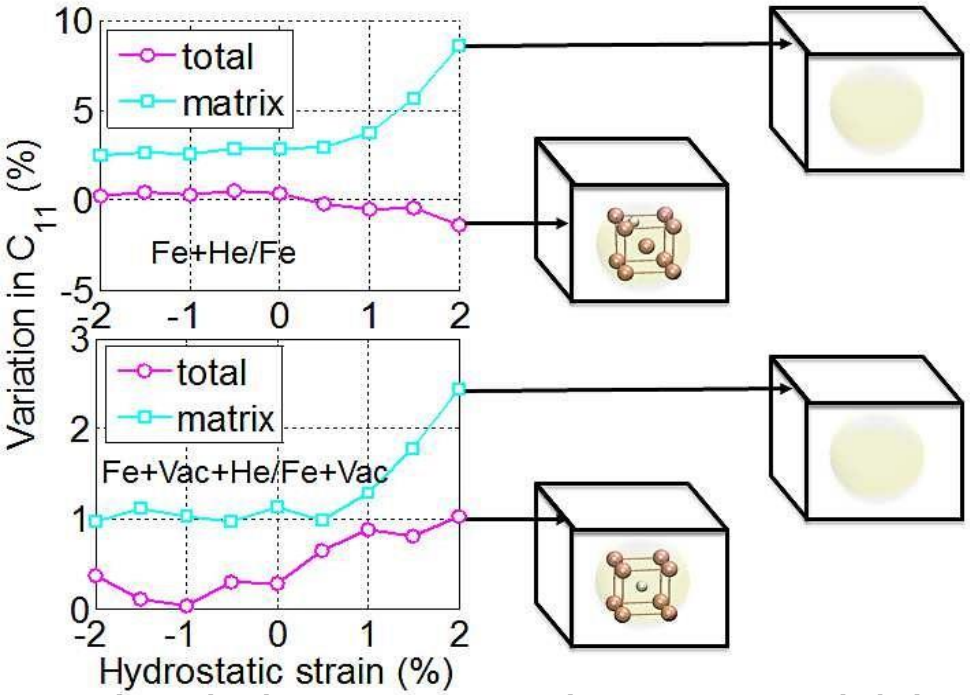

Figure 20. Helium induced variation in C_{11} in Fe and Fe+Vac structures under hydrostatic strain

Fig. 19 presents the C_{11} values for Fe and Fe+Vac lattice under various hydrostatic strain. The influence of helium is not very clearly shown. Therefore, the variation in C_{11} induced by a

single helium atom is shown in Fig. 19. In the case of Fe+He lattice, the C_{11} value of the total structure (magenta curve) experiences no obvious change in compressive strain range. But with increasing tensile pre-existing strain, C_{11} starts to drop slightly with the addition of helium atom. However, in the Fe matrix (cyan curve) surrounding the helium atom in Fe+1He, C_{11} continues to increase due to the repulsion effect of a helium atom. Such repulsion effect is equivalent to adding an extra compressive strain to the current pre-existing strain state, which increases the C_{11} value of the Fe matrix alone according to Murnaghan equation. Such increase of stiffness in Fe matrix is noted as the hardening effect of helium. Due to the local effect brought by the helium atom, such as elastic bond distortion and electronic interaction, a softening in elastic constants is introduced, such that the total change in C_{11} with pre-existing strain is not in accordance with the change of C_{11} in Fe matrix alone. In Fig. 20, the difference between the two curves is actually a representation of the local softening effect of helium. In Fe+Vac lattice, after a helium atom being introduced, the change of C_{11} in Fe matrix with pre-existing strain also shows an increasing trend as displayed. But the magnitude of increment is much smaller compared to the pure Fe lattice, owing to the relaxation effect from the vacancy. Unlike the Fe+1He case, the C_{11} variation of the total Fe+Vac+1He structure shows a smooth growing trend with pre-existing strain. But the extent of increase is smaller than the C_{11} in Fe matrix surrounding the helium and vacancy, denoting again the softening from the local interaction of the helium.

In our simulation, all the cases above are tested under constant volume, which is highly related to the hardening of the matrix surrounding the helium atom. Due to the phenomenon that a single helium atom may not obviously show the softening effect from local interaction, we also conducted extreme cases in Fe+Vac and Fe+O:Vac+4Ti with multiple helium atoms under zero pre-existing strain, to illustrate the significance of the softening. The maximum number of helium atoms to be introduced into the structures are decided from the previous

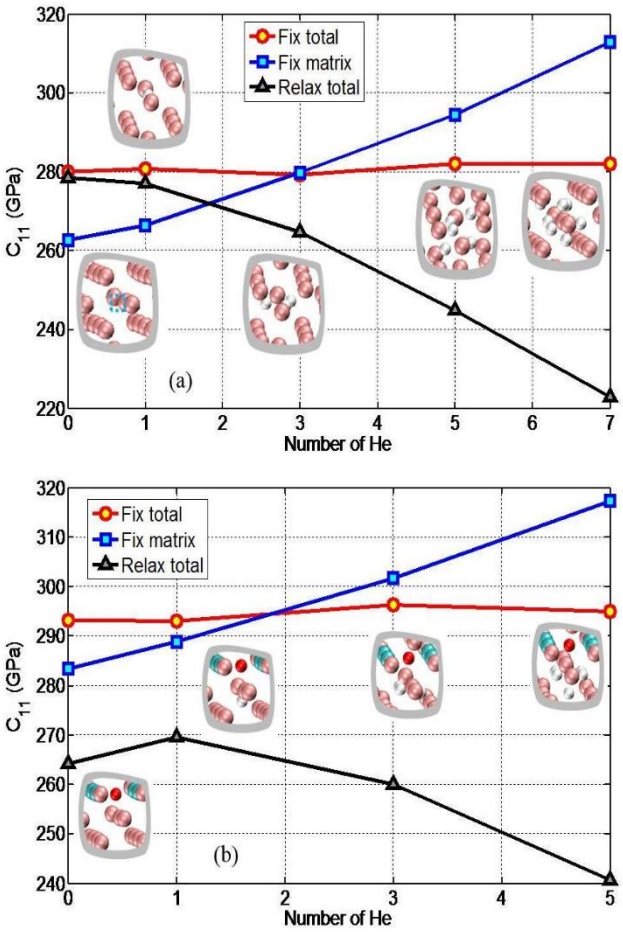

FIG. 21. Elastic constant C11 evolution with different size of helium cluster in (a) Fe+Vac and (b) Fe+O:Vac+4Ti structures. The pink, silver, red, and, green spheres in the in set atomic schematics represent Fe, He, O, and Ti atoms, respectively

work in Ref[s]. The results are shown in Fig. 21. The "Fix total" and "Fix matrix" curves show the evolution of C_{11} in the entire structure containing helium cluster and the ferrite matrix, respectively. C_{11} remains unchanged with the increase of the number of helium atoms. While C_{11} in the ferrite matrix surrounding the helium cluster see a growing trend. Such discrepancy is an evidence that helium cluster can harden the iron matrix under constant volume constraint. At the same time, helium cluster introduces softening effect into the entire structure, which leads to C_{11} remaining almost unchanged. With the removal of constant volume constraint, we estimated the C_{11} values in relaxed Fe+Vac and Fe+O:Vac+4Ti structures with helium cluster. From the "Relax total" curves in Fig. 21, it is observed that the hardening effect of helium cluster vanishes and the entire structures experience an overall softening effect. Such phenomenon denotes again that the elastic behaviors of structures embedded with helium clusters can be largely affected by initial stress states. Irradiation-induced helium bubble can harden Fe matrix under strong constraints of stress states, which can be responsible for the helium-induced embrittlement in structural steel. But the helium bubbles can also result in degradation of mechanical performance given enough time for the structural materials to be relaxed.

Impacts

We found that the presence of tensile initial strain can promote the trapping of helium, while the compressive initial strain weakens the NCs attraction to helium. Regardless of initial strain, vacancies and O:Vac pairs in 14YWT always act as trapping sites of helium atoms, which is to say, even under pressured states, NCs can still control the helium cluster size and distribution. Such understanding of helium solution of 14YWT to external strain is of great significance to its measuring, testing, and design in future applications. Compressive strain hardens Fe matrix while tensile strain softens Fe matrix. The structures under hydrostatic pre-existing strain display weaker elastic anisotropy than the structures under bi-axial pre-existing strain. The elastic anisotropy decreases with increasing pre-existing tensile strain, especially in the case of hydrostatic strain. The existence of solute atom Ti and impurity atom He can induce hardening of Fe matrix in 14YWT under strong constraints. At the same time, helium atoms can degrade the material integrity with local interaction, especially with the removal of strong stress constraints. We have also obtained the polycrystalline elastic parameter for Fe lattice under various initial strain states. Both Young's modulus and shear modulus decrease with increasing pre-existing tensile strain. These results can be used as the input for continuum scale studies such FEA modeling of 14YWT.

3.5 In situ synchrotron tensile investigations on 14YWT and other ODS at room temperature

Nuclear research needs to develop structural materials with excellent resistance to radiations and high-temperatures in order to meet the requirement of the in-core components in the advanced nuclear systems. Oxide dispersion strengthened (ODS) alloys exhibit better radiation

[s] Y. Gan, H. Zhao, D. T. Hoelzer, and D. Yun, "Energetic Study of Helium Cluster Nucleation and Growth in 14YWT through First Principles", Materials, vol:9(1), pp:17, 2016

resistance and high-temperature mechanical properties when compared to conventional ferritic/martensitic steels with the key feature of the small scale particles (micro/nano-particles) distributed within the metal matrix. Depending on the fabrication procedure and heat treatment, the achieved microstructure (phase(s) of the matrix, grain size, type and size of nanoparticles) varies greatly, which leads to an extensive range of ODS alloys that have the potential to be applied to various reactor environments. The material we studied in this project, 14WYT, is one of the newly developed advanced nanostructured ferritic alloys (NFAs), which demonstrated the latest frontier of dispersion strengthened materials. In these NFAs, the ultra-fine (2-5 nm) Y, Ti, and O enriched nanoclusters (NCs) are uniformly distributed within the metallic matrix. Beyond conventional ODS materials, the nanoclusters in 14YWT efficiently decrease the number of micro-cracks that are often generated on the particle-matrix interface when applying external stress on the alloys. 14YWT has shown the highest tensile strength and fracture toughness, and the lowest fracture toughness transition temperature in both irradiated and un-irradiated conditions[t].

Approaches

It is important to characterize the microstructural evolution and understand the role of nanoclusters during in-situ mechanical testing. Therefore, we adopted the high-energy synchrotron X-ray techniques, which has been extensively used to characterize microstructural development during in-situ mechanical or thermal tests for a variety of materials through the diffraction pattern interpretations. In order to understand the influence of nano-features to the microstructural evolution of these ODS and NFAs, we performed the high-energy synchrotron X-ray diffraction

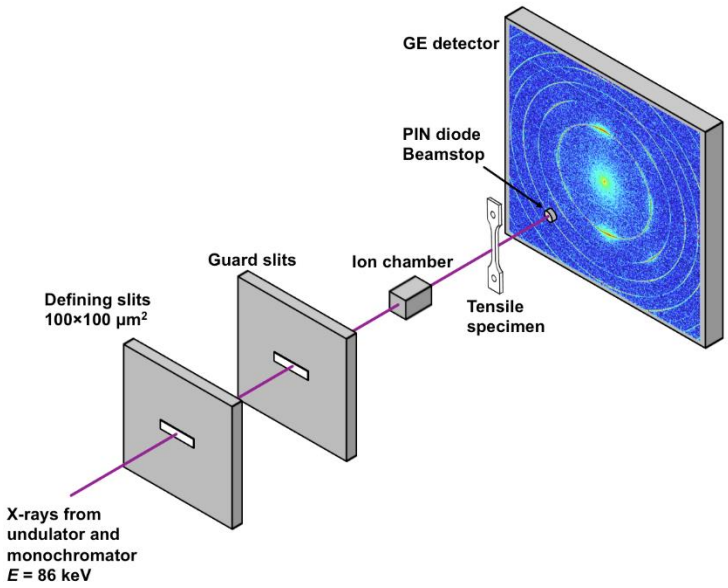

Figure 22. *In-situ* synchrotron X-ray diffraction test setup.

[t] C. A. Williams, E. A. Marquis, A. Cerezo, and G. D.W. Smith, "Nanoscale characterization of ODS–Eurofer 97 steel: An atom-probe tomography study", Journal of Nuclear Materials 400, 37–45 (2013)

tests with respect to three different advanced Fe-based materials including 14YWT, MA957, and 9-Cr ODS.

- The 14YWT (SM170 heat, i.e. SM12d heat in previous publications) alloy is a nanostructured ferritic alloy with the nominal composition: Fe-14Cr-3W-0.4Ti-0.3Y2O3 (wt.%). The average nanoparticle size of the materials is ~4 nm.
- The MA957 is a nanostructured ferritic alloy but with minor compositions of Mo rather than W in 14YWT. The nominal composition of MA957 is 14Cr-1Ti-0.3Mo-0.25Y2O3 (wt.%). The average nanoparticle size of the materials is ~5 nm
- The 9-Cr ODS steel has the nominal composition of Fe-9Cr-0.1C-1.5W-0.2V-0.5Ti-0.35Y2O3 (wt.%). The average nanoparticle size of the materials is ~10 nm.

The in-situ tensile tests with high-energy X-ray diffraction measurements were carried out at the 1-ID beamline at the Advanced Photon Source (APS) at Argonne National Laboratory (ANL). Figure 22 shows the experimental setup. Uniaxial tensile tests were conducted using an MTS closed-loop servo-hydraulic test frame (model 858) with a maximum force of ±15 kN. The SS-J3 type tensile specimens, with a gauge section of 1.2mm×0.75mm×5mm (width×thickness×length), were subjected to increasing uniaxial tensile stresses up to failure with a strain rate of 2×10-4s-1. Diffraction measurements were performed every 7 seconds by using a monochromatic 86keV (λ = 0.0144nm) X-ray beam with a beam size of 100×100 μm^2. The distance between the sample and the detector was ~1.4 m.

Main Results

Figure 23 shows the integrated X-ray diffraction line profile for 14YWT, MA957, and 9-Cr ODS. For the studied alloys, all major diffraction peaks of the α-Fe matrix were identified, while the minor phases including TiN and $Y_2Ti_2O_7$ were only observed in 9-Cr ODS steel. The $Y_2Ti_2O_7$ are the nanoscale particles within the 9-Cr ODS, while TiN is the larger particles within

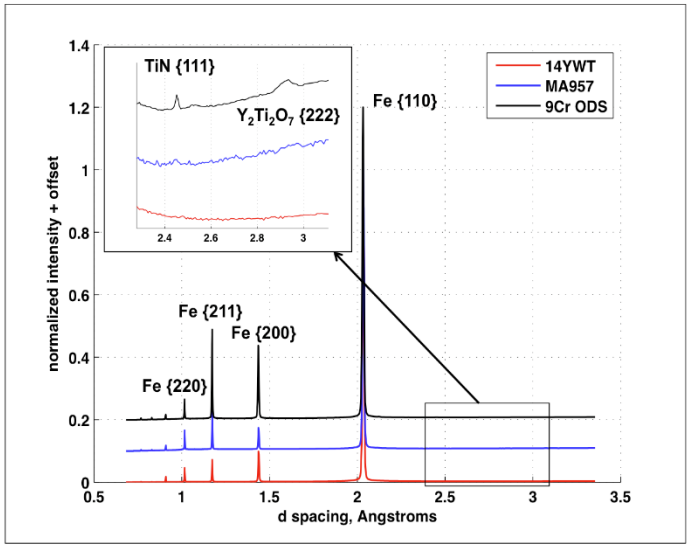

Figure 23. X-ray diffraction line profile of 14YWT, MA957

the steel. In the 9-Cr ODS, the lattice constants for the matrix, TiN, and $Y_2Ti_2O_7$ were measured to be 2.871Å, 4.24 Å, and 10.11Å, respectively. The lattice constant of the matrix for both 14YWT and MA957 was 2.873Å. The Y-Ti-O enriched nanoclusters cannot be identified.

The peak width can be determined from the full-width at half maximum (FWHM) of diffraction peak. The evolutions of FWHM of several α-Fe reflections of the alloys are shown in Fig. 24. Little changes in FWHMs were observed during elastic deformation before sample yielding. After yielding and during the plastic deformation, the diffraction peaks significantly broadened with a sharp increase in the FWHM diagram. This indicated that the peak broadening was mainly caused by microstructural development during plastic deformation. It includes the increase in dislocation population due to strain hardening and changes incoherent scattering volume due to the dislocation structure evolution, e.g. forming of dislocation cell structures. Therefore, in order to understand the role of high-density nano-particles in the material property enhancement of NFA (14YWT), we performed an in-depth investigation and discussion about the nanoparticle distribution and dislocation evolution as follows.

Although all three types of advanced alloys contained nano-scale particles, only those in the 9-Cr ODS were observed in this study using synchrotron X-ray diffraction. **No minor phases were observed in either 14YWT or MA957 in the synchrotron measurement**. (Fig. 23) In the present study, the average size of the nanoparticle/nanocluster is ~4nm, ~5nm, ~10nm for 14YWT, MA957, and 9-Cr ODS, respectively. Since the nanoparticles in the 9-Cr ODS are much larger than those in 14YWT and MA957, many of the nanoparticles are beyond the range of non-stoichiometric limit, i.e. ~15nm. These relatively large particles could be observed by X-ray diffraction due to their stoichiometric nature (the cubic $Y_2Ti_2O_7$ structure). In contrast, the average particle size in the clusters in 14YWT and MA957 are much smaller than the non-stoichiometric limit, thus the majority of nanoparticles are non-stoichiometric, or possibly amorphous, which were invisible in X-ray diffraction. Moreover, the X-ray diffraction volume in this study was 75×105 μm^3, composed of numerous particles. This bulk measurement provided better statistics

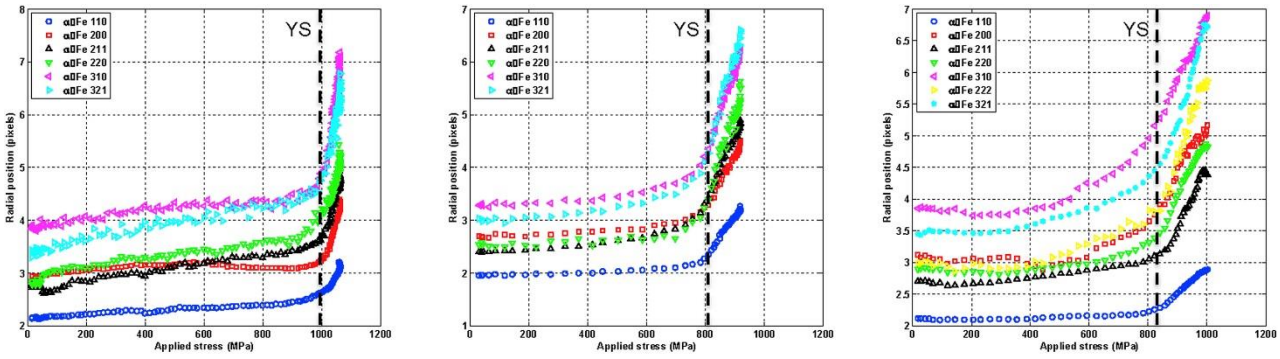

Figure 24. Evolution of FWHM for (a) 14YWT, (b) MA957 and (c) 9-Cr ODS. Yield strength (YS) is indicated by black dashed line. (Note: each pixel is 0.2mm × 0.2 mm)

compared to the smaller scale TEM-based measurements.

Since the micro-strain and coherent scattering volume are two major mechanisms that impact the width of diffraction peaks during deformation. The sum of two broadening mechanisms can be separated by Williamson-Hall (W-H) equation[u]:

$$\Delta K = \frac{0.9}{D} + \Delta K^{D}, \tag{21}$$

where ΔK^{D} is the contribution of micro-strain, and D is the contribution of average grain or particle size to peak broadening. Here, $K = 2\sin\theta/\lambda$, $\Delta K^{D} = 2\cos\theta(\Delta\theta)/\lambda$; θ, λ and $\Delta\theta$ are the diffraction angle, the wavelength of the X-ray, and the FWHM of the diffraction peak, respectively. Ungar et al.[v] and Groma et al.[w] further improved the function of analyzing diffraction line-profile for large crystals containing dislocations, and Eq.21 was then rewritten as:

$$\Delta K = \frac{0.9}{D} + (\pi A b^2/2)^{1/2}\rho^{1/2}\left(KC^{1/2}\right) + (\pi A' b^2/2)^{1/2}Q^{1/2}(K^2C) \tag{22}$$

A new scaling factor C on the line profile, which is termed elastic contrast factor, has been introduced into the W-H equations. A is the parameter determined by the effective outer cutoff radius of the dislocation, is chosen to be 2 for compatibility with a dislocation density of approximately 10^{15} m^{-2}. b is Burgers vector. A' is an adjustable parameter similar to A. Q is a correlation function between two particles in a dislocation ensemble and can be given as the fluctuation of dislocation density. The third term at the right-hand side usually small and is ignored. Eq. 22 is called modified Williamson-Hall equation. By using this equation, the dislocation density can be analyzed by measuring the slope of the fitted plot line.

In this study, the elastic contrast factors of α-Fe were calculated with the elastic constants of Fe (C_{11} = 233GPa, C_{12} = 135GPa and C_{44} = 118GPa)[x]. The elastic contrast factors were then calculated based on most common (110)<111> edge type and <111> screw-type dislocation in body-centered cubic (BCC) materials, and the fraction of dislocation was assumed 50% edge and 50% screw (the influence of this fraction on the dislocation density computation was small). Table 4 shows the calculated elastic contrast factors.

Table 4: Elastic contrast factors (C) of α-Fe reflections

[u] G. K. Williamson and W. H. Hall, "X-ray line broadening from filed aluminum and Wolfram," Acta Metallurgica, vol. 1, pp. 22-31, 1953

[v] T. Ungár and A. Borbély, "The effect of dislocation contrast on x-ray line broadening: A new approach to line profile analysis," Applied Physics Letters, vol. 69, pp. 3173-3175, 1996

[w] I. Groma, T. Ungár, and M. Wilkens, "Asymmetric X-ray line broadening of plastically deformed crystals. I. theory," Journal of applied crystallography, vol. 21, pp. 47-54, 1988

[x] J. A. Rayne and B. S. Chandrasekhar, "Elastic constants of iron from 4.2 to 300 K," Physical Review, vol. 122, pp. 1714-1714, 1961

	{110}	Fe{200}	Fe{211}	Fe{220}	Fe{310}	Fe{222}	Fe{321}	Fe{400}
C	0.1302	0.2578	0.1302	0.1302	0.2119	0.0877	0.1302	0.2578

The dislocation density can be interpreted based on the W-H slope. To show the trend of dislocation density development during the tensile tests, we analyzed the relative dislocation density (ρ') as: $\rho'(\varepsilon) = \rho(\varepsilon)/\ \rho(\varepsilon = 0)$. Figure 25 shows the relative dislocation density as a function of engineering strain during tensile tests. Two different regimes were observed in the evolution of the W-H slope during the tensile tests: (1) Regime I: dislocation density increases significantly (~5 to 6 times of the value before loading) before sample necking ($\sim 0.2\% < \varepsilon < \sim\varepsilon_{UTS}$; ε_{UTS} is the engineering strain at the ultimate tensile strength (UTS)); (2) Regime II: dislocation density stops increasing after necking ($\varepsilon > \varepsilon_{UTS}$). The dislocation behavior in the Regime II was due to the X-ray beam was not probing in the necking region. Although these three types of advanced alloys had similar trends of dislocation density development, the dislocation density in the 9-Cr ODS built up faster than that in either 14YWT or MA957 when plastic deformation was initiated. Recent strengthening modeling on the 14YWT showed that the dispersed-barrier-hardening model provided a better estimation than Orowan by-pass hardening model[y]. This indicated the Y-,Ti-, and O-enriched nanoclusters were sharable, weak particles, compared to the relatively large, hard, and impenetrable nanoparticles in the 9-Cr ODS. The major strengthening

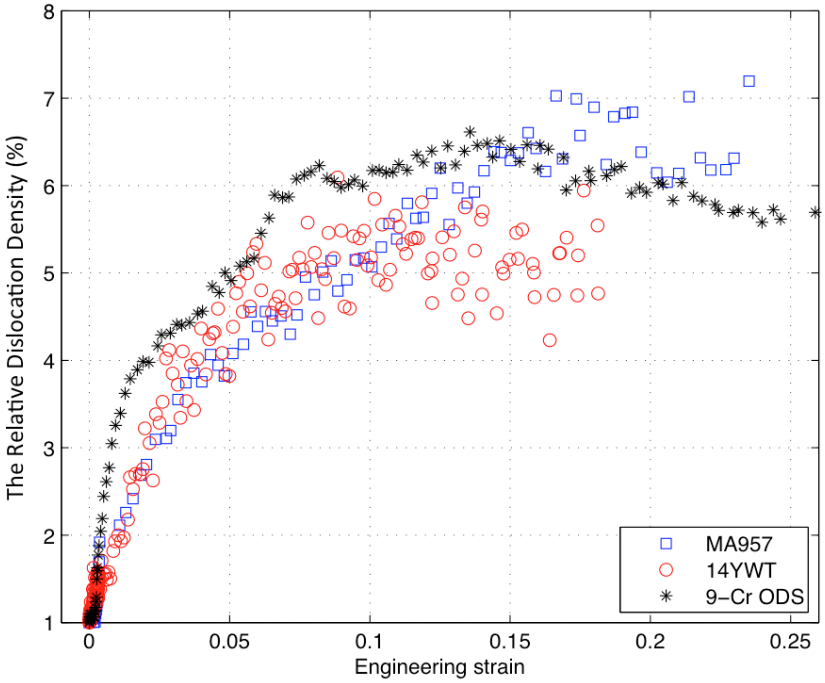

Figure 25. Relative dislocation density (%) vs. engineering strain during

[y] J. H. Kim, T. S. Byun, D. T. Hoelzer, C. H. Park, J. T. Yeom, and J. K. Hong, "Temperature dependence of strengthening mechanisms in the nanostructured ferritic alloy 14YWT: Part II—Mechanistic models and predictions," Materials Science and Engineering: A, vol. 559, pp. 111-118, 2013

mechanism in the 9-Cr ODS can be estimated as Orowan looping that produce a lot of dislocations during plastic deformation. Therefore, the dislocation population increased fastest in the 9-Cr ODS among the studied materials.

Assuming the mean free path of dislocation motion (s) is independent of true strain (ε), the dislocation density relation with a true strain of material can be derived as[z]:

$$\rho(\varepsilon) = \frac{\overline{m}}{bs\Omega} + \left(\rho_0 - \frac{\overline{m}}{bs\Omega}\right) e^{-\Omega\varepsilon}, \tag{23}$$

Where ρ is the dislocation density, ε is the true strain of the material, b is Burgers vector, $\overline{m}$ is Taylor's constant, s is the mean free path of dislocation motion, and Ω is the strain-independent dynamic recovery coefficient which represents the remobilization of immobile dislocations, ρ_0 is the dislocation density at the beginning of the tensile test, i.e. when $\varepsilon = 0$. If the mean free path of dislocation (s) is modeled to be a true strain (ε) dependent, $s(\varepsilon)$ can be given as:

$$s(\varepsilon) = s_f + (s_0 - s_f)e^{-k\varepsilon}, \tag{24}$$

Then the strain-dependent dislocation density can be further derived and simplified as

$$\rho(\varepsilon) = \rho_0 e^{-\Omega\varepsilon} + (e^{-\Omega\varepsilon} - e^{k\varepsilon}) \left(\frac{\overline{m}}{b} \frac{1 + \frac{\Omega + k}{\Omega} \times \frac{e^{k\varepsilon} s_f}{s_f - s_0}}{\frac{k}{(\Omega + k)(s_f - s_0)} + 2} \right). \tag{25}$$

Figure 26 shows the modeling results compared to the experimental data. Both models (for Eq. 23 &13) agree well with experimental data. This suggests the dislocation mean free path (s), which is the average travel distance of dislocations before it was immobilized by interaction with

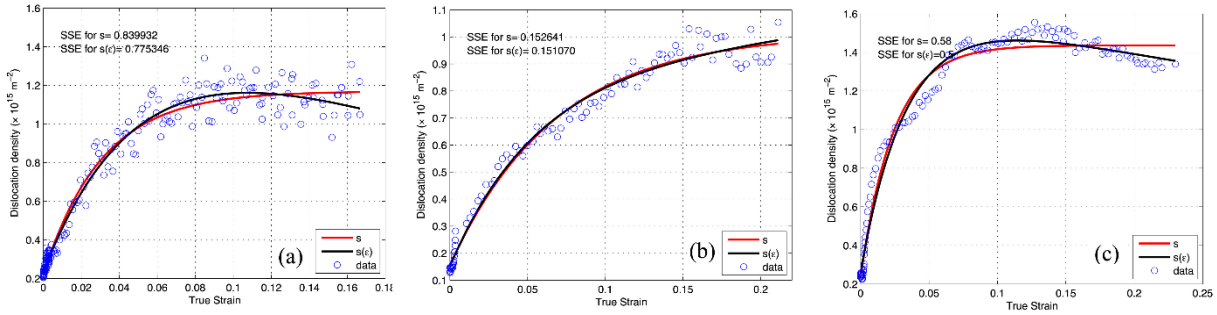

Figure 26. Modeling of dislocation density with true strain for (a) 14YWT, (b) MA957 and (c) 9-Cr ODS. The red curve shows the results based on Eq. 6 (s is ε independent); the black curve shows the results based on Eq. 10 (s is ε dependent)

[z] Y. Bergström, Y. Granbom, and D. Sterkenburg, "A dislocation-based theory for the deformation hardening behavior of DP steels: impact of martensite content and ferrite grain size," Journal of Metallurgy, vol. 2010, 2010

microstructure, did not change significantly during deformation. Nevertheless, the model with strain-dependent dislocation mean free ($s(\varepsilon)$) still exhibits a better consistency with the experimental data (as the smaller value of error sum of squares (SSE)) compared to the model with the constant value of s. Note that the dislocation density was slightly decreasing after necking. This is apparent in the 14YWT and 9-Cr ODS. This decrease in dislocation density might attribute to the behavior of dislocation annihilation during tensile tests, which was mainly due to cross-slip of screw dislocations with opposites signs and has been observed in FCC, HCP and BCC materials. This trend of decrease in dislocation density can only be caught by data fitting using Eq. 25, and thus it should be considered a better model of dislocation density evolution during tensile tests.

Impacts

It is important to adopt high-energy synchrotron X-ray diffraction technique to study the time-resolved lattice strain and dislocation density development during deformation of three advanced nuclear structural materials including 14YWT NFA, MA957 NFA, and 9-Cr ODS steel. We only observed the relatively large nanoparticles in the 9-Cr ODS in the synchrotron X-ray diffraction. The nanoclusters in both 14 YWT and MA957 were invisible in the measurement due to their non-stoichiometric nature. The dislocation density in the 9-Cr ODS built up faster than that in either 14YWT or MA957 when plastic deformation was initiated. This observation implies the Orowan looping is the major strengthening mechanism for the 9-Cr ODS which contains relatively large nanoparticles. In contrast, the major strengthening mechanism in 14 YWT and MA957 is dispersed-barrier-hardening due the ultra-fine but sharable nanoclusters. Based on Bergström's dislocation models, dislocation density evolutions of all studied materials were modeled with two different assumptions: (1) dislocation mean free path was strain independent (i.e. constant value of s); and (2) dislocation mean free path was strain dependent (i.e. s(ε)). Although both models provide good consistency with the dislocation density interpreted from X-ray measurements, only the model with strain dependent s caught the phenomenon of slightly dislocation density decreasing after sample necking.

3.6 Elastic anisotropy and internal strain development in 14YWT during the in situ tensile testing under various temperature conditions

It is important to further understand the mechanical behavior and materials response of 14YWT under both external load and elevated temperature conditions, especially the role of NCs in the material property enhancement.

Approaches

Three different NFAs were employed in the present study: 9YWTV, 14YWT-sm13, and 14YWT-sm170. Both 14YWT-sm13 and 14YWT-sm170 have the same nominal composition: Fe-14Cr-3W-0.4Ti-0.3Y_2O_3 (wt.%), while the average nanoparticle size is slightly different: ~3nm and ~4nm, respectively. The 9YWT has a nominal composition of Fe-9Cr-2W-0.4Ti-0.2V-0.05C-0.3Y_2O_3 with the nanoparticle size of ~5nm.

The in-situ uniaxial tensile tests with high-energy synchrotron X-ray diffraction characterization were conducted at the 1-ID-E hutch beamline at the Advanced Photon Source at Argonne National Laboratory. Uniaxial tensile tests were conducted on an MTS closed-loop servo-hydraulic test frame (model 858) with a maximum force of ±15kN. All the NFAs were machined into the SS-J3 type tensile specimen. During tensile tests, each specimen was subjected to increasing uniaxial tensile stresses up to failure with a strain rate of $2\times10^{-4}s^{-1}$. A monochromatic 72keV X-ray beam, with beam-size of $100\times100\mu m^2$ was used to perform the diffraction measurements. The experiment utilized the "Hydra" detector array, which consists of four area detectors (G1-41RT), for X-ray diffraction measurements. The sample to the detector distance was ~1.7m. The NFAs were tested at various temperatures: RT, 300ºC, 500ºC, and 600ºC using an infra-red furnace at ambient air.

Main Results

The engineering stress-strain diagrams of the three NFA materials tested at different temperatures are shown in Fig. 27. The corresponding ultimate tensile strength (UTS) and the yield strength (YS) are listed in Table 5. Both UTS and YS were observed to decrease with increasing temperature. Among the tested NFAs, 14YWT-sm170 exhibited the best ductility at all studied temperatures; 9YWTV shows the highest strength at all studied temperatures except at 600ºC, and 14YWT-sm13 shows the highest UTS value at 600ºC. Note, from 500ºC to 600ºC, a decrease in UTS of 13.2% for 14YWT-sm13, and a decrease of 11.6% for 14YWT-sm170. However, the reduction in UTS is 49.7% for 9YWTV. Obviously, at a higher temperature regime, 14YWT materials show a higher resistance to temperature softening than 9YWTV.

	T (ºC)	9YWTV	14YWT-sm13	14YWT-sm170
UTS	RT	1.78	1.38	1.10
	300	1.55	1.12	1.00
	500	1.34	0.90	0.59
	600	0.67	0.78	0.52
YS	RT	1.48	1.11	0.87
	300	1.19	0.84	0.73
	500	0.54	0.46	0.50
	600	0.47	0.44	0.37

Table 5: Ultimate Tensile Strengths (UTS) and Yield Strengths (YS) of the NFAs at various temperatures: (units: GPa).

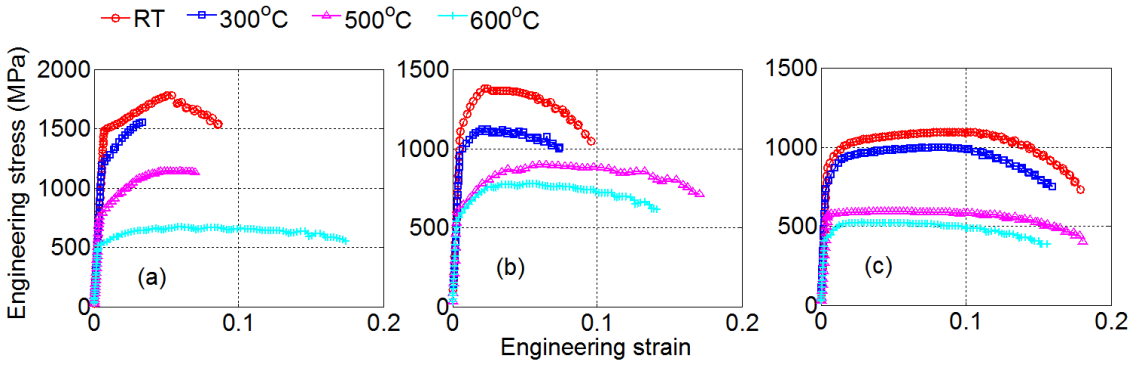

Figure 27. Stress-strain diagrams of the tested NFAs: (a) 9YWTV; (b) 14YWT-sm13; and (c) 14YWT-sm170 at various temperatures.

The lattice strain development of the representative reflections of the NFAs at both room temperature and 600ºC is shown in Fig. 28. The elastic modulus of each reflection can be attained from the slope of lattice strain vs. applied stress curve in the elastic regime. Here, the elastic modulus of each reflection clearly shows a smaller value at 600ºC than that at room temperature. In all the cases, {310} reflection has the lowest elastic modulus. The hook-shaped loading curve was observed in the test of 14YWT-sm170 at low temperatures (Fig. 28(c1)). Similar behavior of internal stress development has been observed in many of the materials with multiple phases: the lattice strain of the metallic matrix slightly decreases during early yielding, but increases afterward until neckingAt 600ºC, temperature softening eliminates this behavior in 14YWT-sm170.

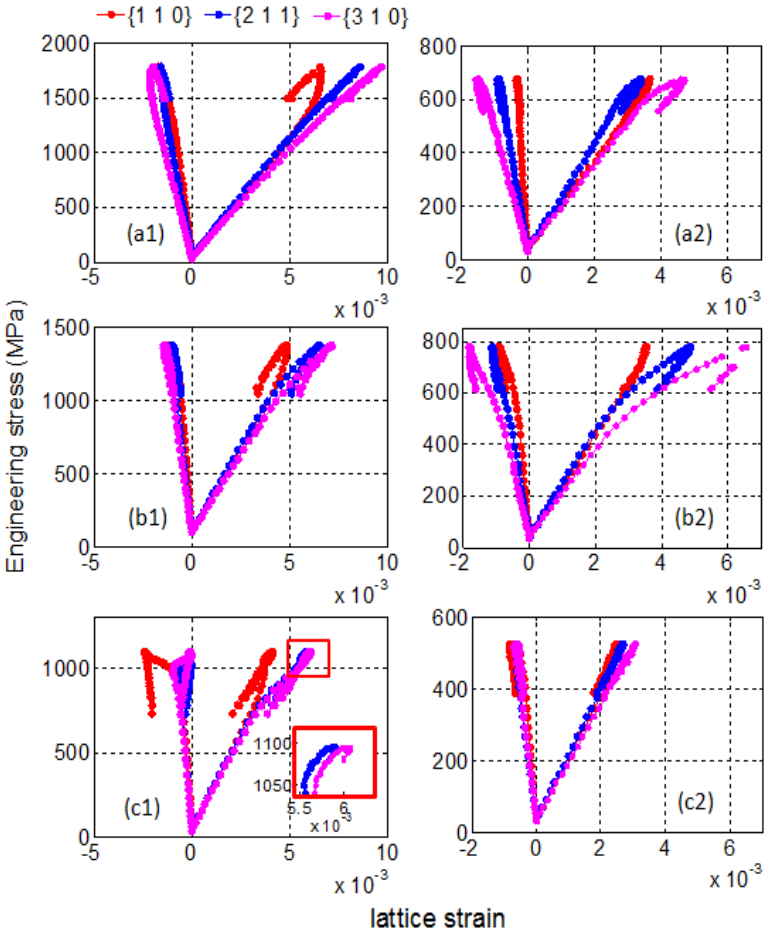

Figure 28. Lattice strain - applied stress relations of three NFAs at room temperature: (a1) 9YWTV; (b1) 14YWT-sm13; (c1) 14YWT-sm170; and at 600°C: (a2) 9YWTV; (b2) 14YWT-sm13; (c2) 14YWT-sm170.

In order to derive important mechanical properties of the NFAs (i.e. Young's modulus and Poisson's ratio) from the results of the in-situ experiments, a reliable model is required to correlate

the single grain behavior and the material bulk responses. Here, we adopted the Kroner's model[aa] to evaluate basic mechanical properties of all three NFAs. Here each grain is defined as an inclusion in a homogeneous matrix with the strain-stress relation of a grain denoted as

$$\sigma_{ij} = \left(C_{ijkl} + r_{ijkl}\left(\Omega\right)\right)\varepsilon_{kl} \text{ or } \varepsilon_{ij} = \left(S_{ijkl} + t_{ijkl}\left(\Omega\right)\right)\sigma_{kl}, \tag{26}$$

where σ_{ij} (or σ_{kl}) and ε_{ij} (or ε_{kl}) are the stress and strain of a grain, respectively; C_{ijkl} and S_{ijkl} are the stiffness and compliance tensors; $r_{ijkl}(\Omega)$ and $t_{ijkl}(\Omega)$ represent the interaction among grains, and Ω is the single grain volume. When we evaluate the overall constitutive relation of the bulk material, the interactions among grains will not manifest themselves by satisfying the following equations

$$\int_D r_{ijkl}\,dD = \int_D t_{ijkl}\,dD = 0\,, \tag{27}$$

where D is the bulk volume. Therefore, the strain-stress relation in bulk materials can be defined as

$$\bar{\sigma}_{ij} = (C_{ijkl})_B \bar{\varepsilon}_{kl} \text{ or } \bar{\varepsilon}_{ij} = (S_{ijkl})_B \bar{\sigma}_{kl} \quad , \tag{28}$$

where $(C_{ijkl})_B$ and $(S_{ijkl})_B$ are bulk stiffness and compliance tensors, respectively. With the elastic-stiffness constants C_{11}, C_{12}, and C_{44}, the shear stiffness $c' = \left(C_{11} - C_{12}\right)/2$ and anisotropy parameter $A = 2C_{44}/\left(C_{11} - C_{12}\right)$ can then be evaluated respectively. According to the definition, the parameter A represents the shear resistance ratio between the elastically hardest orientation and softest orientation, making it the most appropriate measurement for determining the material's elasticity anisotropy.

With respect to the NFAs at two temperature conditions (RT and 600°C), the elastic modulus for each reflection plane was obtained by a linear fitting of the slope of the lattice strain-applied stress curves for each reflection, listed in Table 6. At both RT and 600°C, the {2 2 2} crystallographic planes are the strongest and the {200} crystallographic planes are the weakest. The only exception is 14YWT-sm13 at RT, where elastic modulus of {110} crystallographic planes are slightly larger than that of {222} crystallographic planes, most likely due to measurement errors. The elastic moduli of all the crystallographic planes except {222} are considerably smaller when measured at 600°C than those at RT, whereas {222} crystallographic

[aa] J. D. Eshelby, "The Determination of the Elastic Field of an Ellipsoidal Inclusion, and Related Problems", Proceedings of the Royal Society of London A: Mathematical, Physical and Engineering Sciences 241, 376-396 (1957)

planes develop a larger modulus at 600ºC. Such phenomenon suggests a temperature dependence of the anisotropic behavior of NFAs.

T	Sample	Fitted Elastic modulus E_{hkl} for each peak (GPa)					
		{1 1 0}	{2 0 0}	{2 1 1}	{2 2 0}	{3 1 0}	{2 2 2}
RT	9YWTV	215	181	219	218	196	233
	14YWT-sm13	236	175	214	233	193	231
	14YWT-sm170	231	178	205	236	198	NaN
600 °C	9YWTV	160	129	189	177	153	261
	14YWT-sm13	198	140	201	198	159	244
	14YWT-sm170	172	153	179	179	156	NaN

Table. 6. Elastic modulus for various {*hkl*} reflection; the uncertainty of the values is around ±5GPa.

As the testing temperature increases, materials' softening reflected by the decrease in Young's modulus and the increase in Poisson's ratio was observed in both NFAs (Fig. 29(a, b)). As shown in Fig. 29(c), the shear modulus decreases with the increasing temperature. The temperature dependence of bulk elastic anisotropy was studied through the development of Poisson's ratio as the function of temperature, and the materials' intrinsic mono-crystal elastic anisotropy was determined through the anisotropy parameter *A*. As seen in Fig. 29(d), the anisotropy parameter exhibited very little change in the low-temperature regime (T<400ºC), but

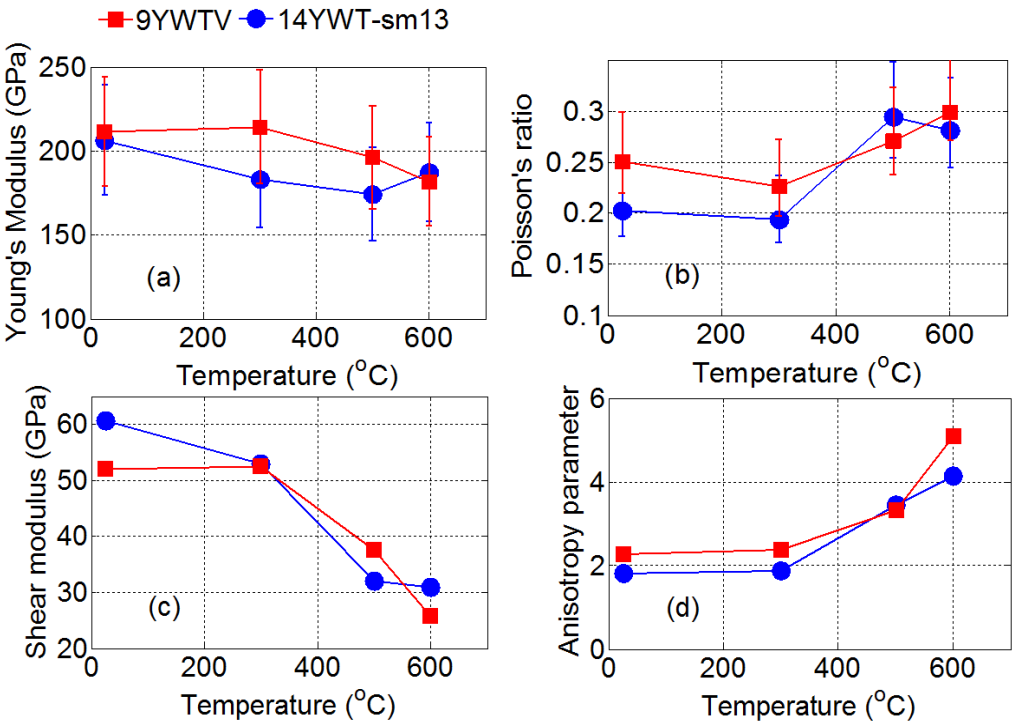

Figure 29. Temperature dependence of elastic mechanical properties for the NFAs: (a) The bulk elastic modulus; (b) Poisson's ratio evolution (c) shear modulus; and (d) anisotropy parameter.

dramatically increased in the high-temperature regime (T>400°C). This increase indicates that the elastic strain response of crystalline in the NFAs develops a higher anisotropy when loaded at high temperatures.

To further investigate the anisotropic behavior of grains orienting in different directions at various temperatures, we calculated the intergranular strains $\Delta\varepsilon^{II}$ to examine the difference between the real lattice strain $\varepsilon_{\{hkl\}}$ and the projected linear elastic strain accordingly, which is defined as

$$\Delta\varepsilon^{II} = \varepsilon_{\{hkl\}} - \sigma/E_{\{hkl\}} \quad . \tag{29}$$

Here, plastic deformation begins within those grains that have orientations that activate their dislocation slip systems upon reaching the point of critical shear stress. Other grains at different orientations, however, sustain more loads in that they continue to respond to the load elastically, which causes a redistribution of stress among these grains. Compressive intergranular strain still accumulates on the grains that first reach the yielding point, while the grains in other orientations that are plastically hard still experience a tensile intergranular strain. Therefore, the onset of the accumulating of compressive intergranular strains of grain aligned in softer orientations is an indication of the elastic anisotropy. As shown in the variation of the compressive intergranular strains with applied stress for {1 1 0} grains in the NFAs (see Fig. 30) the onset of compressive intergranular strain for the sm170 and sm13 14YWT alloys is quite similar at 500°C and 600°C, denoting an insignificant softening at these temperatures. Note that the elastic anisotropy is also restrained in 14YWT while the 9YWTV at 500°C obviously shows a higher yielding point than at 600°C. With the rise in temperature, the compressive intergranular strain starts to accumulate at a much lower external loading value in 9YWTV, indicating an obvious "softening" of the grains.

In order to understand the mechanically strengthening mechanism during the plastic deformation and the loading status for both ferritic matrix and nanoparticles, we calculated the

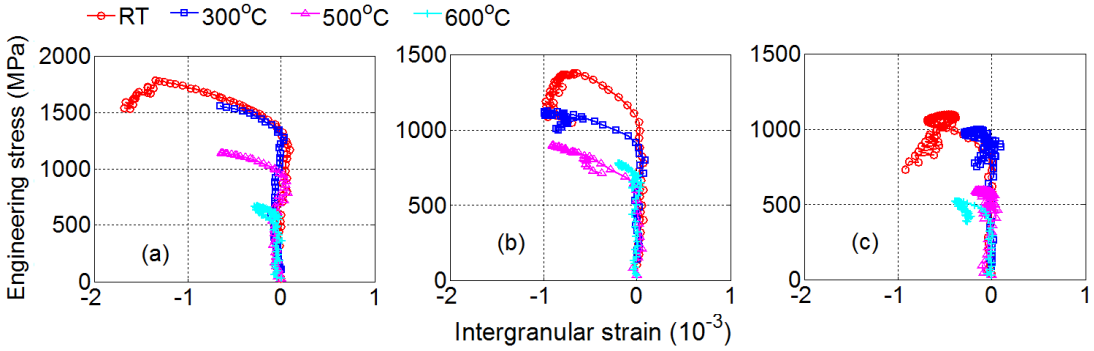

Figure 30. Intergranular strain evolution for the NFAs (a) 9YWTV, (b) 14YWT-sm13, and (c) 14YWT-sm170.

mean internal stress of the matrix and compared it with the externally applied stress. The difference between the internal stress and the externally applied stress refers to the load status of various phases within the NFAs. It can help explain the nanoparticles strengthening effects. The mean internal stress is defined as[bb]:

$$\sigma_{matrix} = \bar{E}\frac{\sum_{hkl} T_{hkl} m_{hkl} E_{hkl} \varepsilon_{hkl}}{\sum_{hkl} T_{hkl} m_{hkl} E_{hkl}}, \tag{30}$$

where $\bar{E}$ is the average Young's modulus of the ferritic matrix, and the fraction term is the mean internal strain defined as a weighted average lattice strain ε_{hkl} for various $\{hkl\}$ reflections. The weighting parameters T_{hkl}, m_{hkl} and E_{hkl} are the texture index, the multiplicity and the stiffness for reflection $\{hkl\}$, respectively. Here, six reflections were included in the calculation: {110},

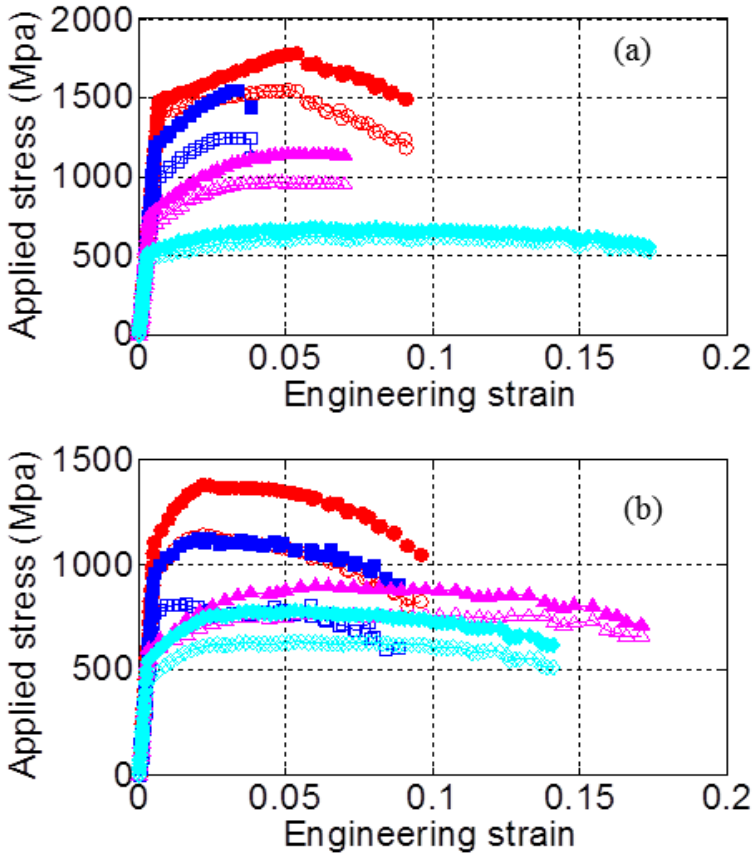

Fig. 31: Comparison of mean internal stress and applied stress for (a) 9YWTV and (b) 14YWT-sm13 at various temperatures (Red: RT; Blue: 300°C; Magenta: 500°C; and Cyan: 600°C). The solid symbols and hollow symbols are applied stresses and internal stresses, respectively.

{200}, {211}, {310}, {321} and {222}. The 9YWTV and 14YWT-sm13 were selected for detailed analysis, and a comparison of mean internal stress developed during the tensile and the externally

[bb] M. R. Daymond, "The determination of a continuum mechanics equivalent elastic strain from the analysis of multiple diffraction peaks", Journal of Applied Physics 96, 4263 (2004)

applied stress are provided in Fig. 31. In all the tests at various temperatures, the mean internal stress was smaller than the actually applied stress after yielding, the difference is caused by the load re-distribution and transfer between phases and grains during plastic deformations. As the main strengthener in these alloys, nanoparticles play an important role in deformation particularly in the load re-distribution in plasticity. For 9YWTV, the difference between mean internal stress and externally applied stress is significant at room temperature, which decreased with an increase in temperature. At 600ºC, this difference is almost negligible (Fig. 31(a)). For 14YWT-sm13, the difference between mean internal stress and externally applied stress was not significant at room temperature, however. Although at 600ºC, the difference was again negligible (Fig. 31(b)). Tthe strengthening of ferritic matrix mainly derives from the function of nanoparticles at room temperature and elevated temperatures. These ultra-fine uniformly distributed nanoparticles pin the dislocation movement, causing the loading transfer between the nanoparticles and the grains, therefore enhancing the strength of the material. A higher temperature dependence of the strengthening for 9YWTV is due to the lack of ultra-fine uniformly distributed nanoparticles, compared to 14YWT-sm13, particularly at the high-temperature regime.

Impacts

In this work, we observed an increase in the elasticity anisotropy in all of the materials studied with an increase in temperature. An analysis of the intergranular strain of 14YWT-sm13 indicated a higher resistance to temperature softening compared to 9YWTV. A further analysis of the strengthening factors indicated differences in the applied and mean internal stress. This variation was due to a higher temperature dependence of the nanoparticle strengthening for 14YWT-sm13 compared to 9YWTV, particularly at the higher temperatures.

4. Dissemination of Results

4. 1 Journal publication

1. Y. Gan, H. Zhao, "Energetic study of Helium interaction at the interface of Fe and TiN/C through first principles theory calculation" (in preparation)
2. Y. Gan, H. Zhao, "First Principles Study of Helium Behavior and Elastic Property Evolution in Pre-strained 14YWT", submitted to Journal of Applied Physics
3. Y. Gan, K. Mo, D. Yun, D. T. Hoelzer, Y. Miao, X. Liu, K.-C. Lan, J.-S. Park, J. Almer, T. Chen, H. Zhao*, "Temperature Effect of Elastic Anisotropy and Internal Strain Development in Advanced Nanostructured Alloys: an in-situ Synchrotron X-ray Investigation". Materials Science and Engineering: A, 692, 53-61, 2017
4. Y. Gan, H. Zhao*, D. T. Hoelzer, D. Yun, "First Principles Calculation of Helium Bubble Nucleation and Growth in 14YWT", Materials, 9(1), 17, 2016 (invited).

5. J-L Lin, K. Mo, D. Yun, Y. Miao, X. Liu, H. Zhao, D. T. Hoelzer, J.-S. Park, J. Almer, G. Zhang, Z. Zhou, J. F. Stubbins, A. M. Yacout, "In situ synchrotron tensile investigations on 14 YWT, MA957, and 9-Cr ODS alloys", Journal of Nuclear Materials, 471, 289-298, 2016.

4.2 Conference Oral Presentation

1. Y. Gan, H. Zhao, "First Principles Study of Elastic Property Evolution in Pre-strained 14YWT", IMECE 2017, Tampa, FL, Nov 3-9, 2017.
2. Y. Gan, H. Zhao, D. Yun, K. Mo, D. Hoelzer, X. Liu, K. Lan, Y. Miao, "Temperature Effect of Microstructural Evolution in Advanced Nanostructured Alloys by in-situ Synchrotron X-ray Diffraction", TMS2016, Nashville, TN, Feb 14-18, 2016
3. K. Mo, D. Yun, J.-L. Lin, Y. Miao, D. Hoelzer, J. Almer, H. Zhao, A. Yacout, "Synchrotron Radiation Study on 14YWT and MA957 Nanostructured Ferritic Alloys", TMS 2015, Orlando, FL, Mar 15-19, 2015.
4. Y. Gan, D. Hoelzer, D. Yun, H. Zhao, "Energetic Study of Helium Bubble Formation in Y-Ti-O Enriched Iron Matrix", TMS 2015, Orlando, FL, Mar 15-19, 2015.
5. H. Zhao, Y. Gan, D. Yun, D. Hoelzer, "Formation and Stability of Y-V-O Enriched Nanoclusters in Fe-Based Alloys: First Principles Theory Study", MRS 2014 Fall, Boston, MA, Nov 30 – Dec 5, 2014.
6. H. Zhao, C-L Fu, Y. Gan, D. Yun, and D. Hoelzer, " Formation and Stability of Y-V-O enriched nanoclusters in Fe-based alloys", Nuclear Material Conference 2014, Clearwater, FL, Oct 27-30, 2014.

4.3 Conference Poster Presentation

1. H. Zhao, Y. Gan, D. Hoelzer, D. Yun, "Material Characterization of Nano-structured Ferritic Alloys: Atomistic Modeling and in situ Synchrotron Testing", Gordon Research Conference, Hong Kong, July 31-August 5, 2017
2. Y. Gan, D. Hoelzer, D. Yun, H. Zhao, "Energetic Study of Helium –Nanoparticle Interaction within Nanostructured Ferritic Alloy", TMS 2017
3. Y. Gan, D. Hoelzer, D. Yun, H. Zhao, "First Principles Theory Calculation of Helium Interaction with Nanoparticles within 14YWT", MRS 2016

4.4 Invited Presentations

1. H. Zhao, "Material Characterization of Nanostructured Ferretic Alloy through Atomistic Modeling", Hong Kong City University, Hong Kong, China (Aug 3rd, 2017). Host: Dr. Xinrui Niu
2. H. Zhao, "Material Characterization of Nanostructured Ferretic Alloy through Atomstic Modeling", University of Washington at Seattle, Seattle, WA, USA (May 3rd, 2016). Host: Dr. Jiangyu Li

3. H. Zhao, "Computational Analysis: Strength of Materials", ANL seminar, Argonne National Laboratory, Argonne, IL, USA (March 27th, 2015). Host: Dr. Di Yun

4.5 Fostered Collaborations

Though the high energy X-Ray diffraction testing at Advanced Photon Source (APS) at Argonne National Laboratory (ANL), the team established new collaborations with Dr. Kun Mo at ANL and Dr. Ruqing Xu at APS. Two new proposals have been developed and submitted to the NEUP program in the year of 2015.

- NEUP-NEET-3: The project title was "Coordinated Investigations of Microstructure Evolution and Mechanical Property Degradation in Advanced Reactor Materials". Dr. Kun Mo was PI and Dr. Huijuan Zhao was one of the co-PIs. The objective was to develop a fundamental understanding of the microstructural evolution and consequent property degradation in Fe-based ferritic/martensitic alloys under irradiation and to provide predictive validation methodology to evaluate materials' in-reactor performance.
- NEUP-NEAMS1.1: The project title was "Xenon Diffusivity in UO_2: Numerical Model Development and Experimental Validation for MARMOT Simulation". Dr. Huijuan Zhao was PI and Dr. Kun Mo and Dr. Ruqing Xu were one of the co-PIs and the no-cost collaborators.

Even though the submitted proposals were not funded, the fostered collaborations will continue with the focus on material modeling and characterizations in the future.

5. Acknowledgement

The team sincerely acknowledge the support from DOE-NEUP-NEAMS program to conduct the above research.